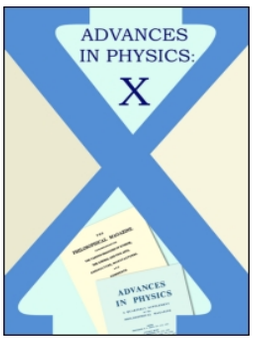

Advances in Physics: X

ISSN: (Print) 2374-6149 (Online) Journal homepage: https://www.tandfonline.com/loi/tapx20

Diffractive metalens: from fundamentals, practical applications to current trends

Wenwei Liu, Hua Cheng, Jianguo Tian & Shuqi Chen

To cite this article: Wenwei Liu, Hua Cheng, Jianguo Tian & Shuqi Chen (2020) Diffractive metalens: from fundamentals, practical applications to current trends, Advances in Physics: X, 5:1, 1742584, DOI: 10.1080/23746149.2020.1742584

To link to this article: https://doi.org/10.1080/23746149.2020.1742584

Published online: 31 Mar 2020.

ADVANCES IN PHYSICS: X
2020, VOL. 5, NO. 1, 1742584
https://doi.org/10.1080/23746149.2020.1742584

Taylor & Francis
Taylor & Francis Group

Diffractive metalens: from fundamentals, practical applications to current trends

Wenwei Liu[a], Hua Cheng[a], Jianguo Tian[a] and Shuqi Chen[a,b,c,d]

[a]The Key Laboratory of Weak Light Nonlinear Photonics, Ministry of Education, School of Physics and TEDA Institute of Applied Physics, Nankai University, Tianjin, China; [b]Renewable Energy Conversion and Storage Center, Nankai University, Tianjin, China; [c]The Collaborative Innovation Center of Extreme Optics, Shanxi University, Taiyuan, Shanxi, China; [d]Collaborative Innovation Center of Light Manipulations and Applications, Shandong Normal University, Jinan, China

ABSTRACT

Traditional optical lenses and the corresponding imaging systems, which are based on the optical paths when light propagates inside the bulky media, usually suffer from the bulky size, Abbe-Rayleigh diffraction restricted resolution, and limited responses to different kinds of incident light. Recently, the burgeoning development of metasurfaces comprised of artificial micro- or nano-structures at the subwavelength scale has drawn more and more attentions of the scientific community due to the intriguing abilities such as efficient light–matter interactions and multi-dimensional manipulation of optical waves, which provide profound potentials to realize functional metalens with an ultrahigh numerical aperture (NA) and with super-resolution focal spots on a compact size. Here, the research motivations, the broad outline and the recent advances of planar diffractive metalens are summarized, including the principles of metalens design, the basic components of metalens, and the development of metalens systems. Various approaches to remove the focusing aberrations are presented, which is the essential condition to realize metalens objectives and microscopy. Different types of novel metalenses are revealed, such as label-free sub-resolution metalens, nonlinear metalens, artificial intelligence-aided metalens, multifunctional metalens and reconfigurable metalens. Challenges and future goals are also presented at the end the review.

ARTICLE HISTORY
Received 26 November 2019
Accepted 9 March 2020

KEYWORDS
Metasurfaces; diffractive optical metalens; flat optical elements; multifunction; sub-diffraction limit

CONTACT Shuqi Chen schen@nankai.edu.cn; Hua Cheng hcheng@nankai.edu.cn The Key Laboratory of Weak Light Nonlinear Photonics, Ministry of Education, School of Physics and TEDA Institute of Applied Physics, Nankai University, Tianjin 300071, China

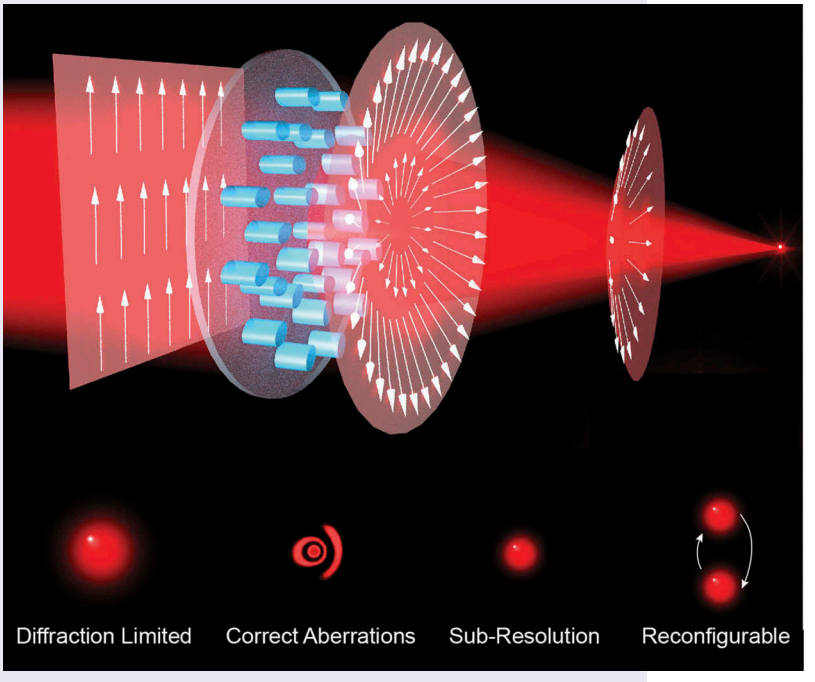

1. Introduction

Optical lens is one of the cores in optical systems, such as telescopes, microscopes, spectrometers, and is widely investigated throughout the history of optics and photonics. Traditional optical lens is developed by engineering transparent media or reflective metals to control the optical path of electromagnetic waves (EMWs), according to the laws of ray optics and wave optics developed by Snell, Fermat, Fresnel, Kirchhoff, and many other pioneers [1]. Although great achievements have been made by using such optical-path-based method, the challenges and drawbacks also arise as the rapid increment of the density of optical information. For example, traditional optical equipment is inevitably bulky compared with electronic circuits, which can even integrate much more components [2,3]. Such bulky size strikingly increases the cost and mass of the optical systems. Another challenge is the lack of multi-dimensional manipulation of optical fields, which confines the development of multifunctional optical devices and the investigation of new optical effects [2,4,5]. Traditional optical devices are also restricted by the Abbe-Rayleigh diffraction limit of about half of the operating wavelength [6]. In the past decades, researchers have developed different methods to increase the optical spatial resolutions, such as near-field scanning optical microscopy [7], far-field fluorescence-based microscopy [8–11], and label-free far-field microscopy [12–14].

However, such methods still suffer from specific limitations and are suitable for certain scenarios.

Metasurfaces, which consist of numerous planar artificial building blocks, provide a wide platform for controlling light in ways that would not be possible with natural materials [15–18]. Such artificial building blocks at the subwavelength scale can interact strongly with the incident light, leading to efficient and versatile resonances in the near-field region, such as electric dipole [19], magnetic dipole [20], toroidal dipole [21], and anapole resonances [22]. By elaborately tailoring the geometry of each building block, one can locally modulate the abrupt phase change [23,24], polarization [25,26], reflection/transmission/absorption [27–30], and the combinations of these optical dimensions [4,31–35] pixel by pixel, which results in many intriguing phenomena and devices such as anomalous refraction [36,37], photonic spin Hall effect [38], Cherenkov surface plasmon wakes [39], special beams generation [40,41], polarization converters [42], and waveguide modes converters [43]. In the past decade, researchers have exploited various kinds of materials to serve as metasurface building blocks. For example, metallic nanostructures are much smaller than the working wavelength, and the induced surface current is a facile tool to control the local resonances [44–49]. Compared with metallic nanostructures, the dielectric scatterer is larger and the height is even comparable with the operating wavelength due to the Mie scattering effect [50–52]. However, the working efficiency of dielectric nanostructures is high compared with plasmonic nanostructures since there is no intrinsic thermal loss, and the dielectric nanostructures could easily combine electric and magnetic dipole resonances within a single structure [53–57]. The two-dimensional (2D) materials such as graphene, WS_2, MoS_2 are also widely investigated due to the intrinsic surface effects and the van der Waals interactions [58–62]. In the past several years, researchers have exploited the realization of metasurface in a broad electromagnetic region, such as the optical [63], infrared [64], terahertz [65], and gigahertz wavebands [66]. The abundant resonances and building blocks provide revolutionary tools to modulate the wavefront of optical fields, and could totally change the optical lens designs on the metasurface platform, namely metalens.

Here, a review of the metalens design and the potential applications is given from the perspective of EMWs interference and coupling. We summarize the current research hotspots and the main challenges of metalens in engineering photonics. In Section 2, we discuss the fundamentals of the metalens design, including the physical principles and the design criteria. In Section 3, we summarize the schemes to realize basic metalens component, such as achromatic metalens and sub-resolution metalens. Complex metalens combinations and systems are discussed in Section 4 to exemplify the distinguished significances and potentials in future photonic applications. An outlook

presenting our opinions on the future trends and challenges in metalens is provided in the last section to guide the future development of metalens.

2. Fundamentals of diffractive metalens

In principle, all the metalens design could be classified into two categories, i.e. the building blocks design and diffractive paths design. As mentioned in the introduction part, the subwavelength building blocks provide efficient light–matter interactions which guarantees EMWs behave far different from that in natural materials. In the focusing area, the EMWs follow the diffraction theory because the metalens usually works in isotropic media.

2.1 Design principles of metalens

In 2011, F. Capasso's group proposed to locally control the phase abrupt of EMWs using the V-shaped nanostructures and realized generalized laws of reflection and refraction, which makes metasurface a significant platform to manipulate the wavefront of EMWs [15]. This group also realized a metalens in the near-infrared region, which opened up the possibilities of high-performance lenses in a flat surface [67]. The phase abrupt is decided by the local modes or local resonances of the nanostructures such as the electromagnetic dipole resonances [37] and Fabry-Perot cavity resonances [68]. Generally, the radiated power of the resonant nanostructures could be calculated by the sum of the multipole moments [21,69,70]:

$$I = \frac{2\omega^4}{3c^2}|P|^2 + \frac{2\omega^4}{3c^4}|M|^2 + \frac{4\omega^5}{3c^5}(P.T) + \frac{2\omega^6}{3c^5}|T|^2 + \frac{\omega^6}{5c^5}\sum|Q_{\alpha\beta}|^2 + \frac{\omega^6}{40c^5}\sum|M_{\alpha\beta}|^2 + O\left(\frac{1}{c^5}\right), \tag{2.1}$$

where P, M, T, $Q_{\alpha\beta}$, $M_{\alpha\beta}$ are defined as the electric dipole, magnetic dipole, toroidal dipole, electric quadrupole, magnetic quadrupole, respectively. Thus, each location of the metasurface could be viewed as an independent wavelet similar to that described by the Huygens-Fresnel principle, no matter whether there are near-field coupling between nanostructures or not. The diffraction field could be written with the Rayleigh-Sommerfeld theory [71]:

$$u(x,y,z) = -\frac{1}{2\pi}\int_{\infty} U(x_0,y_0)g(x-x_0,y-y_0,z,\lambda)\mathrm{d}x_0\mathrm{d}y_0, \tag{2.2}$$

where $g(x,y,z,\lambda) = \exp(inkr)\cdot(ink-1/r)\cdot z/r^2$ is the propagation kernel, and n is the refractive index of the background isotropic medium. Specifically, for metalens, which could convert the incident planar

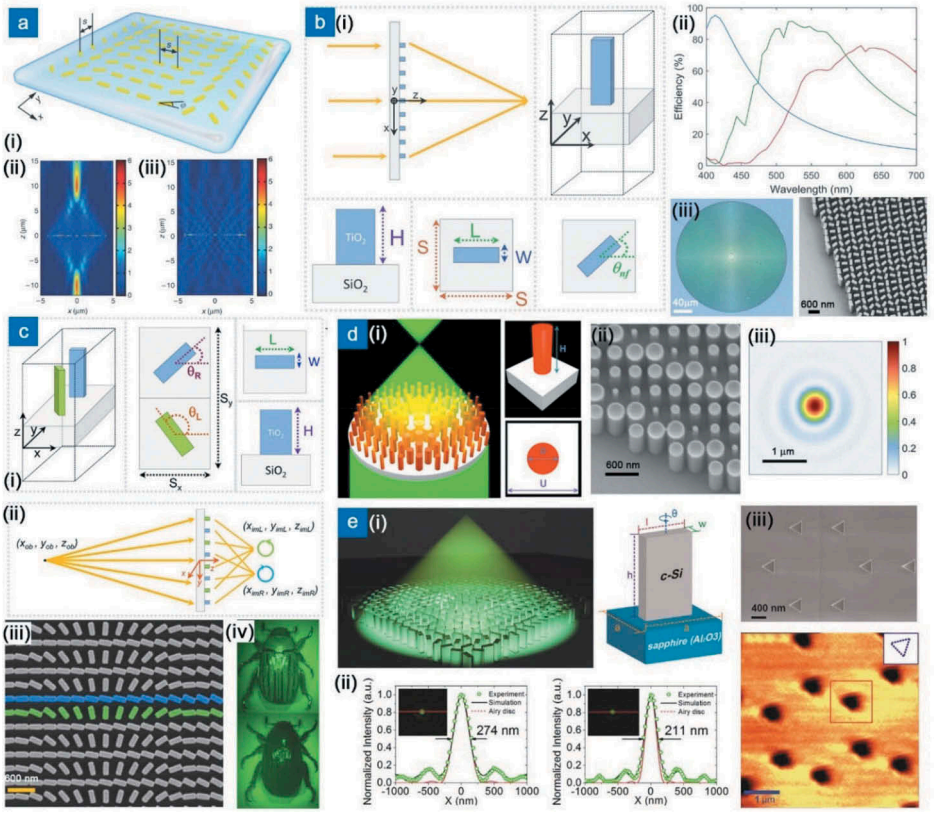

Figure 1. Designs of different kinds of Metalenses. (a) a(i) Bipolar plasmonic metalens realized by P-B phase. Simulated intensity of a(ii) LCP detection for RCP incident light and a(iii) RCP detection for LCP incident light. (b) b(i) Schematic of the high-efficiency dielectric metalens composed of TiO_2 nanofins. b(ii) Simulated polarization conversion efficiency of the dielectric unit cells working at three different wavelengths. b(iii) The optical image and the SEM micrograph of the fabricated dielectric metalens. (c) c(i) The building blocks and design strategy of the chiral metalens. The blue and green nanofins belong to two kinds of metalenses to focus RCP light and LCP light. c(ii) The metalens can focus LCP and RCP light at different locations. c(iii) The SEM micrograph of the fabricated chiral metalens, with two different dielectric building blocks false-colored. c(iv) The images of a beetle, Chrysina gloriosa, under LCP/RCP incident light. (d) d(i) Schematic and the unit cell of the polarization-insensitive metalens operating in transmission mode. d(ii) The SEM micrograph of the metalens. d(iii) Measured intensity near the focal spot at the operating wavelength of 532 nm. (e) e(i) Schematic and the c-Si building blocks of the ultrahigh NA metalens. e(ii) Comparison between the measured, simulated intensity profiles and the Airy disc profile of the focal spot (left) in air and (right) in immersion oil. e(iii) SEM micrograph and the experimental scanned image using the metalens. The length of the triangle is 320 nm. Figures reproduced from: (a) ref [75], reproduced under the terms of the Creative Commons Attribution-NonCommercial-NoDerivative Works 3.0 Unported License (http://creativecommons.org/licenses/by-nc-nd/3.0/), Copyright 2012, Nature Publishing Group; (b) ref [81] Copyright 2016, American Association for the Advancement of Science; (c) ref [88] Copyright 2016, American Chemical Society; (d) ref [72] Copyright 2016, American Chemical Society; (e) ref [94] Copyright 2018, American Chemical Society.

wavefront to the spherical one, the phase abrupt at each location of the metalens needs to be [67]:

$$\phi(x,y) = \frac{2\pi}{\lambda}\left(\sqrt{(x^2+y^2)+f^2} - f\right), \tag{2.3}$$

where f is the working focal length of the metalens. The hyperbolic phase distribution described in Equation (2.3) means a large phase gradient when the metalens is large. Thus, the size of the unit cell U should be small enough to avoid high orders of diffraction, and should meet the Nyquist sampling criterion [72,73]:

$$U < \frac{\lambda}{2NA}, \tag{2.4}$$

where $NA = \max\{NA_{\text{obj}}, NA_{\text{image}}\}$, and NA_{obj}, NA_{image} are the numerical apertures in the object and image planes, respectively. Especially, NA is the numerical aperture of the metalens for normal incidence.

2.2 Typical designs of metalens

One of the intriguing phase types is Pancharatnam–Berry (P-B) phase, which is based on the spatial symmetry of the local fields of the nanostructures [74]. As shown in Figure 1(a), the phase abrupt in each unit cell is $\phi = -2\sigma\theta$, where $\sigma = \pm 1$ represents the left/right-handed circularly polarized (LCP/RCP) light, respectively, and θ is the orientation angle of the nanostructure. Note here the phase ϕ denotes the cross-polarization state of the incident light, namely the anomalous light. Since the phase of the anomalous light becomes its opposite number when changing the helicity of the incident light, the metalens serves as a convex lens and a convex lens for LCP and RCP incident light, respectively [75]. For the polarizer-based plasmonic antennas, no more than 25% of the incident LCP/RCP light could be cross-polarized due to the absorption and mirror effect of the polarizer [49]. Although half-wave-plate-based plasmonic antennas could realize cross-polarization conversion with high efficiency, multi-layered designs or fabrication-challenging building blocks are often required, especially for the transmission mode [76,77]. On the other hand, by employing dielectric high-ratio nanofins, which induces intrinsic waveguide modes and makes the dielectric antenna a half-wave-plate-like component, the cross-polarization conversion efficiency reaches about 100% [78–82]. By utilizing such nanofins, a high-efficiency metalens is realized in the visible (Figure 1(b)). The scanning electron microscope (SEM) image in Figure 1(b iii) shows that the nanofins could be fabricated with high precision following the atomic layer deposition

method [83]. One of the main advantages of such high-ratio nanofins is that it only requires high refractive index and low thermal loss in the operating wavelengths, such as silicon in the infrared and titanium oxide in the visible. Thus, the building blocks are easily designed for different wavebands. The engineering materials, especially silicon, are compatible with the commercial semiconductor industry and the complementary metal-oxide–semiconductor (CMOS) techniques [54,84–87].

Since the P-B-phase-based metalens is dependent on the incident polarization state, chiral metalens can be realized by elaborate arrangement of the nanofin building blocks [88]. As shown in Figure 1(c), two nanofins arrays were arranged in a single metalens, resulting in different locations of the focal spots for LCP and RCP incident light. This kind of chiral metalens could map the circular dichroism of the object, such as a Chrysina gloriosa whose exoskeleton shows different reflectivity for LCP and RCP incident light. Recently, the intrinsic chiro-optical activity has been widely investigated and the working efficiency reaches a really high level [89,90]. The high-ratio dielectric nanopillars can be designed working in all the polarization states, just as a traditional lens, since the waveguide mode in the dielectric nanofins covers the phase range from 0 to 2π by adjusting the effective refractive index of the waveguide [55,72,83,91–93]. A finite difference time domain analysis of the dielectric nanopillars was performed to demonstrate the waveguide modes, leading to polarization-insensitive metalens working in the visible (Figure 1(d)). An ultrahigh NA (reaching 1.48) metalens with efficiency of 48% can also be realized with a c-Si-based nanobrick array, which operates in immersion liquid with refractive index of 1.512 [94]. As shown in Figure 1(e), a diffraction limited ultrahigh resolution was realized (about 0.40λ) at the operating wavelength of 532 nm, and the measured full with at half maximum (FWHM) reaches 211 nm in the immersion liquid.

3. Basic diffractive metalens components

Although many novel metalenses have been realized as introduced in Section 2, the basic components of metalenses still need to be expanded such as the achromatic metalens and sub-resolution metalens for realistic applications. In this section, we will discuss the realization of aberrations-correcting metalens, sub-resolution metalens, nonlinear metalens, and artificial intelligence (AI) aided metalens.

3.1 Correcting monochromatic aberrations

In traditional optics, the devices suffer from five types of monochromatic aberrations, i.e. the spherical aberration, comas, astigmatism, field

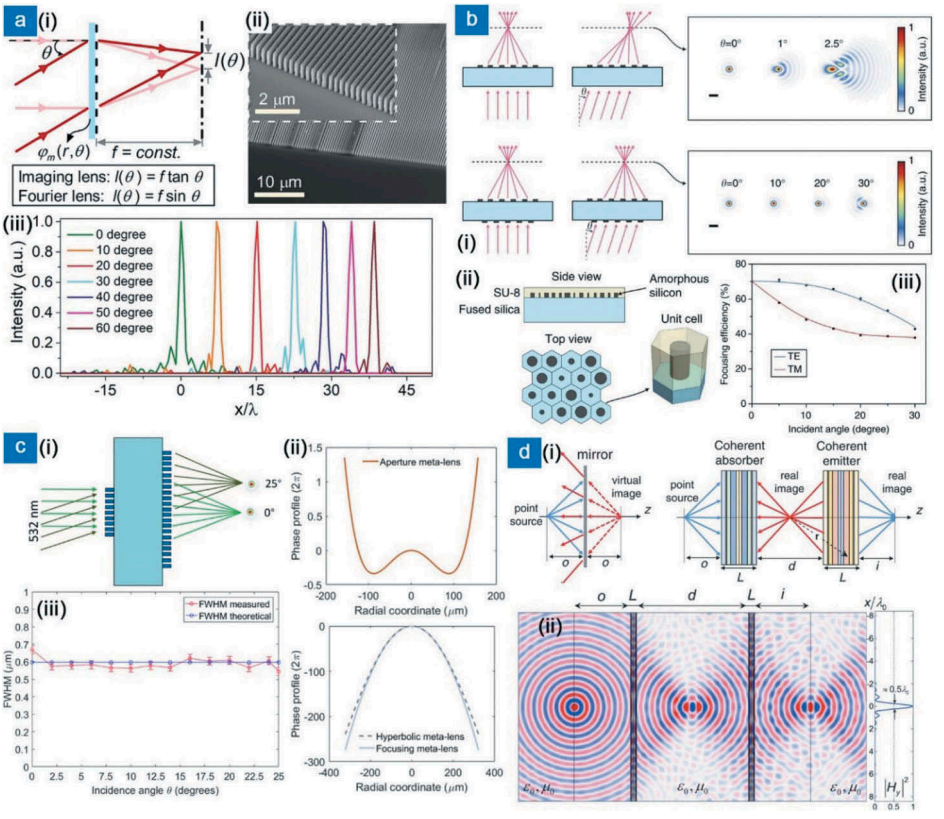

Figure 2. Metalens designs for monochromatic aberrations. (a) a(i) For different incident angles the foci shift differs for an imaging metalens and a Fourier metalens. a(ii) SEM micrograph of the fabricated Fourier metalens operating in the infrared region. a(iii) Measured intensity profiles near the focal points for different incident angles at the operating wavelength of 1500 nm. (b) b(i) The singlet metalens suffers from spherical aberration for off-axis incident light, which could be removed by the doublet design to increase the working field-of-view to 60 degree. b(ii) A schematic of the dielectric metalens, with the a-Si nanoposts covered by a layer of SU-8 polymer. b(iii) Measured focusing efficiency of the doublet metalens for TE and TM incident light. (c) c(i) Schematic illustration of the doublet metalens working in the visible. c(ii) The phase profiles required by the aperture metalens to correct the spherical aberrations, and the phase profiles of the focusing metalens. c(iii) A comparison between the theoretical and measured FWHMs for different incident angles. (d) d(i) Comparison between two kinds of monochromatic aberration-free imaging. (left) Case one: a plane mirror with perfect imaging; (right) Case two: the designed nonlocal PT-symmetric metalens composed of a pair of coherent absorber and a coherent emitter. d(ii) A snapshot of the magnetic field distribution of the designed PT-symmetric metalens at the steady state. Figures reproduced from: (a) ref [95] Copyright 2018, WILEY-VCH; (b) ref [102], reproduced under a Creative Commons Attribution 4.0 International License (http://creativecommons.org/licenses/by/4.0), Copyright 2016, Nature Publishing Group; (c) ref [103] Copyright 2017, American Chemical Society; (d) ref [107] Copyright 2016, American Physical Society.

curvature, and image distortion. Generally, if one could accurately control the local phase function of each unit cell as deduced in Ref [95], the focusing metalens will be perfect:

$$\Phi_{\mathrm{m}}(r,\theta) = \gamma \sin\theta + \sqrt{1+\left(\gamma - \frac{l(\theta)}{f}\right)^2} - \sqrt{1+\left(\frac{l(\theta)}{f}\right)^2}, \tag{3.1}$$

where $\Phi_{\mathrm{m}}(r,\theta) = -\phi_m/k_0 f$, $\gamma = r/f$, is the normalized phase and radius. By applying this formula and the waveguide modes in a-Si microstructures, a Fourier metalens working under 0° to 60° incidence was realized (Figure 2(a)). Different from conventional optical media, the resonance-based metalens provides a possibility for local control of the phase function of the building blocks in the form of Equation (3.1). However, currently, the arbitrary control of the phase function over the incident angles is still challenging, and researchers were seeking for efficient methods to modulate the angular dispersions of the nanostructures [96–101]. M. Qiu et al. proposed an analysis method to quantitatively describe the angular dispersion of the metasurfaces in the terahertz waveband [96]. Another method to correct the monochromatic aberrations was to learn from the traditional method: using a corrector and forming a doublet metalens. As shown in Figure 2(b), A. Faraon's group in detail studied the focusing of on-axis and off-axis light for a singlet metalens, and proposed to correct the off-axis aberrations by introducing another metalens on the other side of the substrate [102]. The phase profiles took the form of Taylor expansion:

$$\phi(\rho) = \sum_{n=1}^{5} a_n \left(\frac{\rho}{R}\right)^{2n}, \tag{3.2}$$

where ρ is the radial coordinate and R is the radius of the metalens. The coefficients a_n were optimized for minimizing the size of the focal spot at incident angles from −30° to 30°. The phase profiles were obtained through the ray-tracing technique provided by the commercial optical design software, Zemax, and the working efficiency reached more than 40% for both TE and TM incidence in the field-of-view of 60°×60°. In this work, the hydrogenated a-Si was utilized to decrease the thermal loss of a-Si at 850 nm incidence, and a layer of SU-8 polymer is applied to protect the fabricated samples. By applying a similar design scheme, i.e. using both the aperture metalens and the focusing metalens, a doublet metalens working in the visible was realized with the titanium dioxide nanofins [103] (Figure 2(c)).

The abovementioned methods are based on ray-tracing techniques. Another intriguing and practical method is to utilize the negative refraction effects, which was realized in 2000 by J. Pendry [104]. The negative refraction effect results from the simultaneous electric and magnetic resonances, which is a basic condition to realize negative permittivity and permeability [105,106]. As shown in Figure 2(d), A. Alù's group realized a Parity-Time symmetry-based metasurface that operates in all-angle to remove the monochromatic

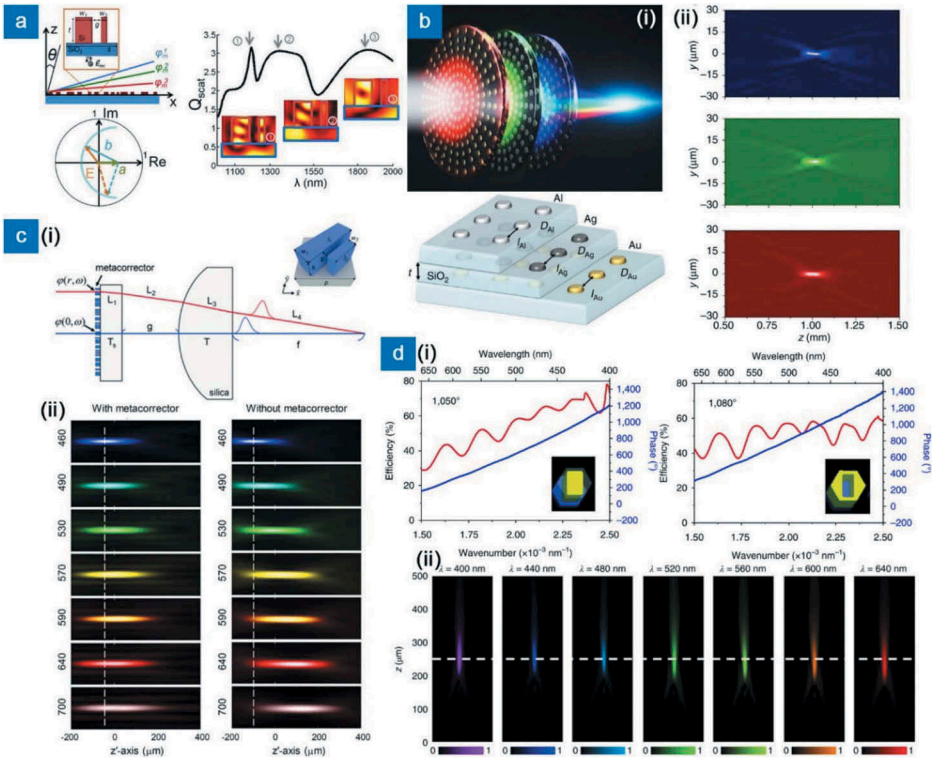

Figure 3. Achromatic metalenses designed in the near infrared and in the visible wavebands. (a) Achromatic metalens designed in three discrete wavelengths of 1300 nm, 1550 nm, and 1800 nm using the dispersive phase compensation. (b) b(i) Schematic illustration of the three-layer Fresnel binary metalens, each layer of which could focus a different working wavelength on the same focal spot. b(ii) Measured intensity distributions for 450 nm, 550 nm, and 650 nm incident light. (c) c(i) A metacorrector used to correct the chromatic aberration of the spherical lens. By meeting the calculated conditions of the group delay and the group delay dispersion, one can realize the required broadband achromatic metacorrector. c(ii) Measured focusing intensity in linear scale for different incident wavelengths with and without the metacorrector. (d) d(i) The circularly polarized conversion efficiency and the phase compensation of (left) 1050° and (right) 1080° with different GaN nanopillar cavities. d(ii) Measured focusing intensity distribution in the waveband from 400 nm to 660 nm. Figures reproduced from: (a) ref [108], Copyright 2015, American Association for the Advancement of Science; (b) ref [109], reproduced under a Creative Commons Attribution 4.0 International License (http://creativecommons.org/licenses/by/4.0), Copyright 2017, Nature Publishing Group; (**c**) ref [121], Copyright 2018, American Chemical Society; (d) ref [123], Copyright 2018, Nature Publishing Group.

aberrations [107]. A single plane mirror is aberration-free because the diffraction limited virtual image is the same as the point source. Similarly, a coherent absorber and a coherent emitter were proposed to mimic the imaging of a single plane mirror. By realizing the scattering matrix:

$$S = c\begin{pmatrix} \mathrm{m1} & +1 \\ +1 & \mathrm{m1} \end{pmatrix}, \tag{3.3}$$

which is independent of the incident angles, the device could absorb the complete angular spectra of the incident waves when illuminated from both sides with a specific phase relation. By employing both of the coherent absorber and the coherent emitter, a Parity-Time-symmetry-based metalens that can work in all angles was realized.

3.2 Achromatic metalens

The chromatic aberration results from the phase accumulation when light at different wavelengths travels and is widely observed in traditional optical devices such as gratings, lenses, prisms, and wave plates. In the metalens scheme, the chromatic aberration could be corrected in principle by elaborate control of the resonances at different working wavelengths. As shown in Figure 3(a), three wavelengths of 1300 nm, 1550 nm, and 1800 nm were optimized to remove the chromatic aberration by the nano-waveguide couplers [108], which means the phase function should satisfy:

$$\phi_m(r,\lambda) = -\frac{2\pi}{\lambda} l(r) + C(\lambda), \tag{3.4}$$

where $l(r)$ contains the optical wavefront information of the device, such as a beam deflector or a lens, and $C(\lambda)$ contains the phase compensation for different wavelengths. Another type of achromatic metalens is to combine different layers of metalenses into one, in which each layer of metalens serves as a single metalens operating at an independent wavelength. As shown in Figure 3(b), each of the layers (composed of three different metals: gold, silver, and aluminum) servers as a narrow band Fresnel binary zone plate, and the three zone plates were designed with the same focal length [109]. Such few-layer metasurfaces have been widely investigated recently due to the abundant interlayer interactions and the feasible fabrication processes [52,110–115]. Since the required phase compensation lies in a wide range, the achromatic metalens working in a wide bandwidth is not easy to realize [116–119]. To achieve the broadband achromatic metalens, a continuous phase compensation is needed in the working waveband:

$$\phi_{lens}(r,\lambda) = \phi(r,\lambda_{\max}) + \Delta\phi(r,\lambda), \tag{3.5}$$

$$\Delta\phi(r,\lambda) = -\left[2\pi\left(\sqrt{r^2+f^2}-f\right)\right]\left(\frac{1}{\lambda}-\frac{1}{\lambda_{\max}}\right), \tag{3.6}$$

where the former part in Equation (3.5) describes the basic focusing phase profiles and is independent on the operating wavelength λ, and the latter part in Equation (3.5) requires elaborate design of the resonators. By employing plasmonic nanostructures the chromatic aberration over

a broadband region from 1200 to 1680 nm for circularly polarized light was corrected with the efficiency of about 12% [120].

Another method to realize the chromatic phase compensation is to investigate the group delay $\partial\boldsymbol{\phi}(r,\omega)/\partial\omega$ and the group delay dispersion $\partial^2\boldsymbol{\phi}(r,\omega)/\partial\omega^2$, which directly describes the phase dispersion over different operating wavelengths [121]. As shown in Figure 3(c), a metacorrector was utilized in the wavepacket tracing, and the chromatic aberration could be corrected by meeting the wavelength-dependent phase profile:

$$\boldsymbol{\phi}(r,\omega) = \boldsymbol{\phi}(r,\omega_d) + \left.\frac{\partial\boldsymbol{\phi}}{\partial\omega}\right|_{\omega=\omega_d}(\omega-\omega_d) + \left.\frac{\partial^2\boldsymbol{\phi}}{\partial\omega^2}\right|_{\omega=\omega_d}(\omega-\omega_d)^2, \qquad (3.7)$$

where ω_{d} is the design frequency. With the designed titanium dioxide metacorrector, the achromatic lens works well from 460 nm to 700 nm incidence. Researchers also demonstrated the dispersion-tailored achromatic metalens with working wavelengths from 460 nm to 670 nm with a working NA of 0.2 for focusing and a working NA of 0.02 for imaging [122], and the working efficiency was about 20%. Another successful material in the visible to realize achromatic metalens was the gallium nitride. As shown in Figure 3(d), taking advantages of the strong resonances of the solid and the inverse gallium nitride nanopillars, a large phase dispersion was realized in the visible, from 400 nm to 640 nm [123]. The working NA was 0.106, and the operating efficiency was about 50%. The NA of the designed achromatic metalenses was low because for large NA the required phase compensation will also become a function of the incident angles, which makes the design procedure a time-consuming work.

3.3 Sub-resolution metalens

Metalens also suffers from Abbe-Rayleigh diffraction limit, just as the traditional optical lens does. The advantages or superiorities of metalens lie in multi-dimensional manipulations of the optical fields, which makes metalens an intuitive method to realize super-oscillatory sub-resolution focusing without fluorescence labeling [124]. Since M. Berry and S. Popescu demonstrated that the diffraction from a grating could create ultra-small localization of EMWs in far-field region [125], researchers have exploited different methods to realize super-oscillation such as using radially polarized light [126–129] and binary apertures [130–132]. In 2009, N. Zheludev's group realized sub-resolution focusing by judicious design of the optical mask which created constructive interference of EMWs in a far-field distance, without the need for evanescent fields [133]. The fields of the EMWs were given by a limited series of the orthogonal prolate spheroidal wave functions $\psi_n(c,x)$:

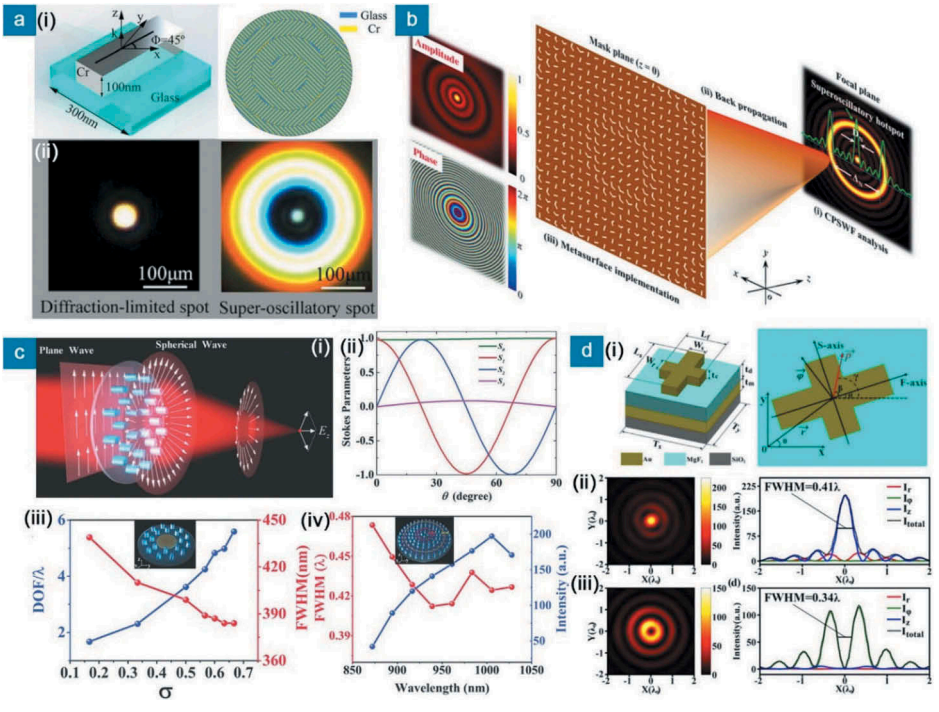

Figure 4. Label-free sub-resolution metalens. (a) a(i) Phase-based binary super-oscillatory metasurface. The plasmonic metasurface combined with a traditional lens could generate a super-oscillatory focal spot. a(ii) The light intensity of a diffraction-limited spot and the super-oscillatory focal spot with a high-intensity side lobe around it. (b) With simultaneous intensity and phase modulation, a limited series of circular prolate spherical wave functions were realized. A super-oscillatory focal hotspot of 0.33λ was achieved at the focal plane. (c) c(i) Schematic illustration of the dielectric super-oscillatory metalens that can focus the radially polarized light at the focal plane. c(ii) The calculated Stokes parameters for different orientations of the elliptic nanopillar, showing that the polarization angle is dependent on the orientation angle. c(iii) The calculated DOF and FWHM as a function of σ, which is defined as the ratio of the diameter of the central metallic filter and the total metalens. The operating wavelength is 915 nm. Inset: Schematic illustration of the sub-resolution metalens with a circular metallic filter. c(iv) The calculated FWHM and the intensity of the focal spot as a function of the incident wavelength. In this case, there is not a circular metallic filter but an additional phase distribution as illustrated in the inset. (d) d(i) Schematic of the quarter-wave metamirrors for generating sub-resolution vector fields. d(ii) Intensity distributions of the total light and each component for longitudinally polarized focal spot. d(iii) Intensity distributions of the total light and each component for azimuthally polarized focal spot. Figures reproduced from: (a) ref [134], Copyright 2018, WILEY-VCH; (b) ref [135], Copyright 2019, American Physical Society; (**c**) ref [137], Copyright 2018, WILEY-VCH; (d) ref [138], Copyright 2019, Optical Society of America.

$$h_N(x) = \sum_{n=0}^{n=N} a_n(c)\psi_n(c,x), \tag{3.8}$$

Theoretically, the FWHM of the sub-resolution focus could be arbitrarily small by sacrificing the working efficiency and the field-of-view.

As shown in Figure 4(a), a P-B-phase-based binary phase plate was realized with the Cr nanorods [134]. Since the P-B phase is symmetry-induced and is wavelength independent, the designed super-oscillatory phase plate is broadband. A strong white focus with size of 0.625 times of the Airy spot was observed, surrounded by a bright lobe ring pattern. By employing both amplitude and phase manipulation, a metalens with NA as high as 1.52 and the focal size as small as 0.33λ was demonstrated [135]. The schematic illustration was shown in Figure 4(b) with a super-oscillatory hot spot in the center of the focal plane. The amplitude and phase manipulation were realized by the plasmonic V-shaped nano-antennas. The working efficiency of the sub-resolution metalens could be further improved by employing dielectric nanopillars. It has been demonstrated that the high-index dielectric nanopillars with tailored geometric size and different orientation angels could realize simultaneous and full control over the polarization states and phase with near-unitary transmission [24,32,33,136]. Such characteristic enables the dielectric nanopillars to simultaneously realize sub-resolution focusing and radially polarized light generation [137]. As shown in Figure 4(c), the incident linearly polarized light was converted to a radially polarized focusing light by the proposed silicon nanopillar arrays. The researchers employed two methods to realize sub-resolution light fields. (1) By placing a metallic aperture in the center of the metalens to block the low spatial frequency component, the FWHM of the focal spot reaches 0.419λ and the depth of focus (DOF) reaches 5.6λ, forming a longitudinally polarized light needle at the focal point. (2) By employing an additional phase distribution, the FWHM of the focal spot is 0.42λ. The size of the foci could be further reduced by delicate design of the aperture or the additional phase distribution. A broadband quarter-wave-plate-based sub-resolution metalens was also realized in the reflection mode (Figure 4(d)). The cross-shaped plasmonic nano-antennas generates azimuthally or longitudinally polarized focusing light, and forms sub-resolution hot spot and hollow spot [138]. Based on the outstanding abilities of multi-dimensional manipulation of the optical fields, metalens may realize high-performance label-free sub-resolution focusing, and further achieve practical imaging techniques someday.

3.4 Nonlinear metalens

Nonlinear metalens is based on the intrinsic nonlinearity of the materials. When tailoring the geometry of the building blocks, the nonlinear optical responses are different from those of the linear media. For example, the P-B phase depends not only on the incident polarization states and the symmetry of the nanostructures but also on the order of the nonlinearity [139–145]. As demonstrated in Ref [141], the geometric phases are $(n\text{-}1)\sigma\theta$ and $(n\text{-}1)\sigma\theta$ for the nth harmonic generation with the same or opposite circular polarization to that of the fundamental EMWs. Such continuous

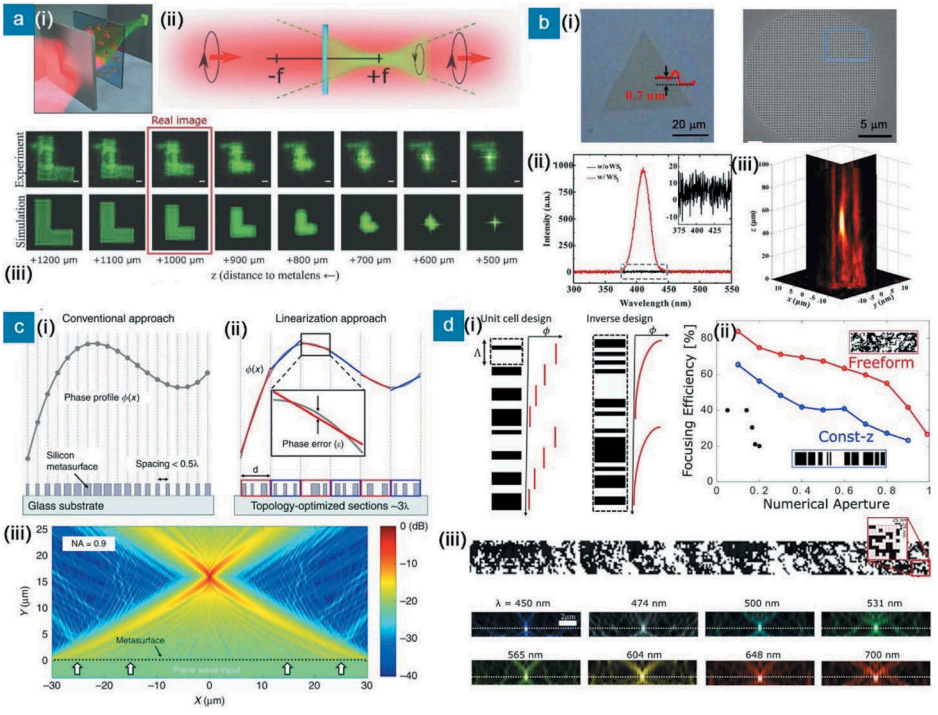

Figure 5. Nonlinear and AI aided metalens. (a) a(i) Schematic illustration of the plasmonic nonlinear metalens composed of C3 nanoantennas. a(ii) SHG focusing and the measurement. The incident RCP fundamental waves could be converted to LCP focused SHG signals. a(iii) Measured and simulated image formation behind the nonlinear metalens. (b) b(i) The optical and SEM micrograph of (left) the WS_2 monolayer and (right) the fabricated gold metasurface. b(ii) The SHG emission spectra of the gold metasurface with and without the WS_2 monolayer. b(iii) Nonlinear focusing intensity of the WS_2-gold hybrid metalens. (c) c(i) Conventional metalens design with calculation and optimization of the phase in each unit cell. c(ii) The proposed topology-optimized metalens design with division section of d = ~3λ. c(iii) Simulated intensity distribution of the silicon metalens with an NA of 0.9 and with the focusing efficiency exceeding 90%. (d) d(i) Comparison between the conventional unit cell design and the proposed inverse design. d(ii) Comparison of the efficiency between the inverse-designed metalenses using 'freeform' and 'constant-z' geometries, as a function of the working NA. d(iii) The designed near-unity-NA broadband achromatic metalens and the focusing profiles realized by the proposed inverse design of the 'freeform' geometry. Figures reproduced from: (a) ref [148], Copyright 2018, WILEY-VCH; (b) ref [153], Copyright 2018, American Chemical Society; (c) ref [164], Copyright 2019, Nature Publishing Group; (d) ref [165], Copyright 2020, Optical Society of America.

control of the nonlinear P-B phase could be utilized to manipulate the wavefront the nonlinear light [146,147]. A C3 symmetric nanoantenna array was applied to realize the second harmonic generation (SHG) and the P-B phase manipulation (Figure 5(a)). The simulated localized surface plasmon polariton was at 1064 nm, and the measured resonances was slightly shifted to 1085 nm. By controlling the polarization states of the

SHG signals, the focused SHG light was observed, and further the SHG imaging of an L-shaped aperture was captured by the CCD camera [148]. Taking advantages of the strong local resonances and symmetries of the nanostructures, many novel nonlinear phenomena and devices could be realized such as the rotational nonlinear Doppler effect [149], simultaneous control of the spin and orbital momentum of SHG light [150], high harmonic generation [151], and a broadband optical frequency mixer [152]. Another intriguing platform to investigate the nonlinear photonics is the 2D materials. For example, a WS_2 layer was combined with the gold nanohole arrays to form a WS_2-Au hybrid metasurface (Figure 5(b)). A large SHG susceptibility of ~10^{-1} nm/V was realized at the working wavelength of 810 nm, and the SHG susceptibility was 2 or 3 orders of magnitude larger than the typical plasmonic metasurface [153]. By controlling the P-B phase of the hybrid metasurface, the SHG focusing was also achieved. The WS_2-Au hybrid metasurface also provides a feasible platform for coherent steering of nonlinear chiral valley photons, which may benefit the realization of nonlinear quantum and valleytronic nanodevices [154]. Nowadays, the development of nonlinear metasurfaces and nonlinear wavefront-shaping devices are growing faster and faster, which may enable the practical applications such as super-resolution imaging, quantum optical information processing, and biosensing.

3.5 Artificial intelligence aided metalens

In the past decade, the geometric effects and the intrinsic light–matter interaction modes of the subwavelength nanostructures were widely investigated, which greatly boosted the rapid development of nano-photonics. However, with the striking increment of the multi-dimensional parameter spaces in the metasurfaces designs, the realization of some high-performance metasurfaces becomes time-consuming, such as the high-NA, high-efficiency metalens, and the ultra-wideband multifunctional meta-devices. Recently, the development of AI techniques has become a research hot spot, and enables novel microwave and photonic devices, which may relieve the researchers from tedious trials and errors-testing works [155–163]. For example, a topology-optimized method was applied to optimize the phase design of the metalens [164]. As shown in Figure 5(c), conventional metalens is realized by designing the nanostructures in the unit cell (smaller than 0.5λ), while the proposed topology-design aims at optimizing the nanostructures in a section of ~3λ. Thus, the designing restriction on the size is relieved by about an order of magnitude, leading to the improvement of the working efficiency (exceeding 90%) of the high-NA and large-area metalens. Another intriguing high-NA achromatic metalens was achieved recently by an inverse design [165]. As mentioned in

Section 3.2, the high-NA achromatic metalens is hard to realize because the unit-cell-based design leads to rapid variations of the phases for different operating wavelengths when the working NA is large. Researchers employed the inverse design that did not have unit cell limit. The total scattering and diffractive properties of the device was incorporated (Figure 5(d)). Considering the electric fields at the exit plane:

$$\mathbf{E}(\mathbf{x}) = \frac{1}{A}\sum_i c_i \hat{\varepsilon}_i e^{i\mathbf{k}_i\cdot\mathbf{x}} = \sum_i c_i \mathbf{E}_i(\mathbf{x}), \tag{3.9}$$

and the time-reversed field at the desired focal point:

$$\mathcal{F} = \frac{1}{2}\sum_i \left| c_i^* c_i^{tar} \right|^2, \tag{3.10}$$

a 'mimimax' optimization was applied over the geometrical degrees of freedom and the frequency domain:

$$\max_{geo}[\min_{\omega} \mathcal{F}(\mathbf{E})], \tag{3.11}$$

Two design methods based on the inverse design, namely constant-z geometry and freeform geometry, were compared by the focusing efficiency (Figure 5(d ii)). Specifically, the freeform inverse design was employed to realize the near-unity-NA (0.99) achromatic metalens, which works well across the visible waveband from 450 nm to 700 nm (Figure 5(e iii)).

4. Applications of metalens systems

As introduced in the previous sections, metalens has been systematically investigated in the past several years and many novel types of metalenses arise. Nowadays, almost every kind of traditional lens has a counterpart in the metalens research area. Researchers also developed metalens systems, some of which are really fascinating and promising. In this section, we will discuss the applications of metalens systems, including the multifunctional metalens, tunable metalens, and the metalens cameras/microscopy.

4.1 Multifunctional metalens

Multifunctional metasurface is a kind of metadevice that can execute concurrent tasks, such as multi-vortices beams generation [166–170], multi-holography generation [32,97,171–173], and other metasurfaces containing several functions [92,174,175]. Generally, the multifunctional metalens is also based on the phase manipulation of the EMWs. For example, by taking the $n\pi$ phase locations of the hyperbolic phase distribution, a convex-concave double lens could be realized (Figure 6(a)) [73]. The simulated

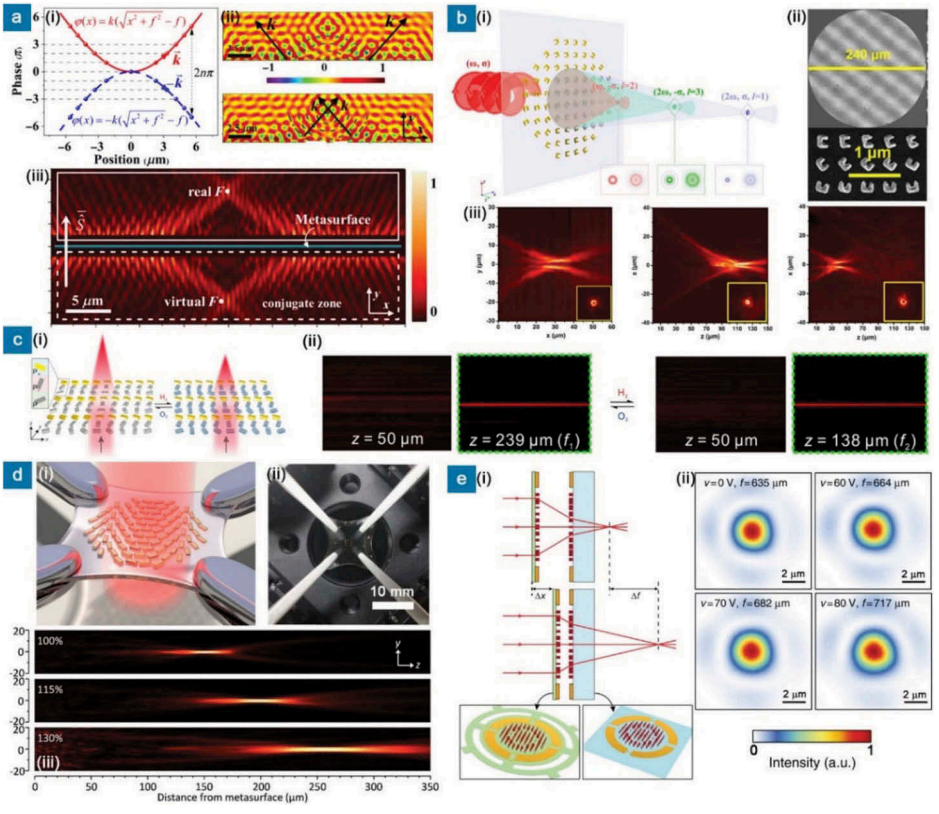

Figure 6. Multifunctional metalens and reconfigurable metalens. (a) a(i) Designed phase profiles of the convex-concave double metalens for any incident polarization state. a(ii) The simulated transmitted field distributions, showing the simultaneous focusing and diverging wave front. a(iii) The intensity distribution of the metalens with the real and the virtual focal spots. (b) b(i) The nonlinear metalens that can triple the capacity of optical vortices using nonlinear channels. b(ii) The SEM micrograph of the nonlinear metalens. b(iii) The measured intensity profiles for (left) the fundamental -σ light, (middle) SHG σ light, and (right) SHG -σ light. (c) c(i) Schematic illustration of the dynamic Janus metalens realized by the hydrogenation/dehydrogenation procedure of the magnesium nanorod. c(ii) The measured focusing and defocusing intensity profiles after H_2 and O_2 exposures. (d) d(i) Tunable metalens on a stretchable substrate mounted on four linear translation stages. d(ii) Photograph of the PDMS film with the metalens on it. d(iii) Measured focusing profiles of the metalens for different stretch ratios, which is defined as the final length divided by the initial length. (e) e(i) Schematic of the MEMS-based dielectric metalens with a scanning frequency potentially reaching a few kHz. e(ii) The focusing intensity and focal length of the MEMS doublet metalens at different actuation voltages. Figures reproduced from: (a) ref [73], Copyright 2017, American Physical Society; (b) ref [176], Copyright 2018, WILEY-VCH; (c) ref [191], Copyright 2018, American Chemical Society; (d) ref [195], Copyright 2016, American Chemical Society; (e) ref [196], reproduced under a Creative Commons Attribution 4.0 International License (http://creativecommons.org/licenses/by/4.0), Copyright 2018, Nature Publishing Group.

results illustrate the diverging and focusing wavefronts simultaneously, with the real and virtual focal points at the focal planes. Taking advantages of the different values of the P-B phases for different orders of harmonic

generation [141], researchers have realized focused optical vortices in both linear and nonlinear regions with a single metasurface [176]. As shown in Figure 6(b), the P-B phases for the fundamental EMWs (-σ) and for the SHG signals (σ, and -σ) are $2\sigma\theta$, $\sigma\theta$, and $3\sigma\theta$, respectively, leading to the corresponding focusing with different focal lengths. The differences in the P-B phases also resulted in different topological charges in each channel. Such kind of multifunctional metalens expands the multi-vortices generation to the nonlinear region, and the capacity of information channels were tripled. By combining different metalenses with the segmented [177], or interleaved [178,179] arrangements, multi-foci metalenses that can focus the incident light at different locations were also realized. Such multifunctional metalenses will enable the possibilities for future integrated metalens systems.

4.2 Tunable and reconfigurable metalens

The functions are invariable for most of the metasurfaces and metalenses once they are fabricated. However, it is very useful and cost saving to realize the tunable and reconfigurable metalenses for realistic applications, such as the scanning microscopy and cameras. Today, there are two major methods to realize the tunable metalens.

4.2.1 Inducing the material changes

The geometric parameters of the nanostructures are not easy to be repetitively and reversibly varied, but the phase of the building materials could be changed at certain conditions. For example, germanium antimony telluride ($Ge_2Sb_2Te_5$, GST) is a promising reconfigurable material with a crystallization temperature at about 160°C and a melting temperature of about 600°C [180]. GST has different refractive indices at different phases of crystalline and amorphous states, leading to the dynamic modulation of the transmitted/reflected amplitude/phase [180–186]. By controlling the crystallization fraction of GST, the refractive index can also be continuously modulated between that of the crystalline and the amorphous states [187]. Based on the phase-changing GST layer underneath the nanostructures, a cylindrical bifocal metalens was realized with the focal lengths of 0.5 mm and 1 mm for the amorphous and crystalline states, respectively [188]. Another phase-changing material is vanadium dioxide, which could switch between the metallic and the dielectric phases in multi-wavebands such as in the infrared and the terahertz [189,190]. Recently, the magnesium-based nanorods were employed in a dynamic metalens design [191]. As shown in Figure 6(c), with the hydrogenation and the dehydrogenation processes, the phase distributions were altered from a longer focal length metalens to a shorter one. Graphene, as a typical 2D material whose Fermi level could be changed by controlling the gate voltage or doping,

has been widely investigated due to the potentials as a tunable material [30,59,60,192,193]. The optical indices of such materials could be changed by different inducing methods, which further results in wavefront manipulation of the EMWs.

4.2.2 Varying the working configurations

Another commonly used method to realize tunable metalens is by varying the working configurations of the metalens [194]. With Au nanorod arrays fabricated on a stretchable substrate (a PDMS film), the focal lengths varies when stretching the substrate by four linear translation stages (Figure 6(d)) [195]. However, since the required phase distribution of focusing is not linear, the focusing suffers from some aberrations a little bit when stretching the substrate, leading to the increment of the DOF (Figure 6(d iii)). A. Faraon's group realized a tunable doublet metalens based on the microelectromechanical systems (MEMS) [196]. By applying a voltage to the doublet MEMS metalens, the distance between the two layers of metalens varies, and the focal point also moves a distance away (Figure 6(e)). The monochromatic aberrations could be further removed by a triplet design using the metacorrector as introduced in Ref [102]. Interestingly, the MEMS-based tunable metalens possesses a scanning frequency potentially reaching a few kHz, which is very fascinating in practical scanning and imaging systems.

Researchers also employed the coherent absorption in a plasmonic metalens to control the focal intensity from 'on' to 'off' states [197]. In this configuration, two coherent beams illuminated from the opposite sides of the metalens, and the coherent structured control beam could modify the signal beam by controlling the absorption, leading to a modified focal spot or an eliminated focal spot. To date, full and independent tunable phase manipulation in each unit cell is still challenging, especially for the near infrared and the visible region because the building blocks are only about hundreds of nanometers. Using electrically controlled diodes, the state of each unit cell of the coding metasurface has been switched between '0′ and '1′ in the GHz region [198]. By applying the gate voltage, a graphene-gold hybrid reconfigurable metasurface was also demonstrated which could modulate the phase in a range larger than 230° at a wavelength of 8.50 μm [199].

4.3 Metalens cameras and microscopy

Recently, some intriguing metalens-based techniques have arose, which may benefit the realistic applications of metalens, and may enlighten future developments of novel metalenses. An off-axis metalens was realized as a compact high resolution spectroscopy working in the wavelength range

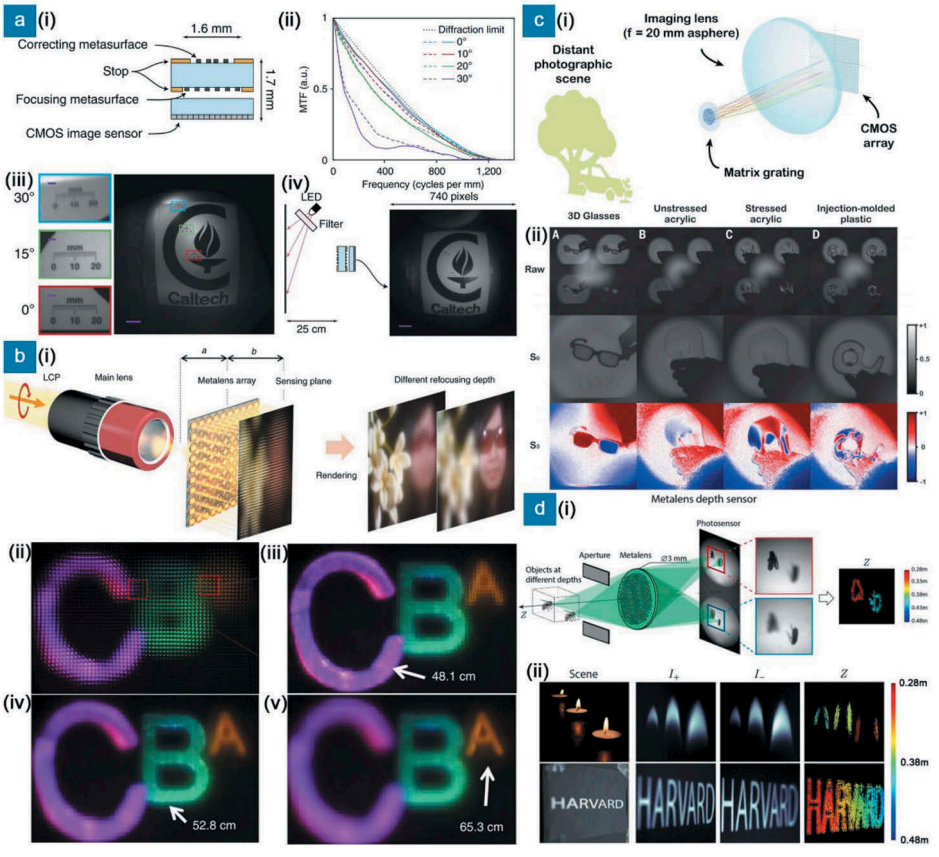

Figure 7. Metalens cameras and microscopy prototypes. (a) a(i) Schematic illustration of the doublet metalens that can correct the monochromatic aberration. The metalens was mounted with a CMOS image sensor with total size of 1.6 mm × 1.6 mm × 1.7 mm. a(ii) The MTFs as a function of the spatial frequency for different incident angles. a(iii) The images taken with the doublet metalens for different viewing angles of 0°, 15°, and 30°. a(iv) The imaging setup and the photograph captured by the miniature doublet metalens. (b) b(i) Schematic illustration of the achromatic light-field camera realized by metalens arrays. b(ii) The raw light-field image captured with the light-field camera. b(iii–v) The final rendered images with focal depths of (iii) 48.1 cm, (iv) 52.8 cm, and (v) 65.3 cm. (c) c(i) Schematic of the full-Stokes polarization camera with a matrix metagrating that can image four diffraction orders with different polarization states onto four spatial quadrants of the CMOS sensor. c(ii) Different photographs taken by the single-shot full-Stokes polarization camera, indicating the birefringence of the object. (d) d(i) Schematic illustration of the metalens depth sensor that can mimic the jumping spider. d(ii) Input images and the output depth maps, which vividly show the depth of the images. The output maps are captured in a single shot. Figures reproduced from: (a) ref [102] Copyright 2016, Nature Publishing Group; (b) ref [202], Copyright 2019, Nature Publishing Group; (c) ref [203], Copyright 2019, American Association for the Advancement of Science; (d) ref [204], Copyright 2019, Proceedings of the National Academy of Sciences of the United States of America.

of 1.1 μm to 1.6 μm [200]. Different from traditional grating-based spectroscopy, the spectral resolution of the metalens is given by:

$$\delta\lambda = \frac{\Delta\lambda}{f\left\{\sin^{-1}\left[\left(1+\frac{\Delta\lambda}{\lambda_d}\right)\sin(\alpha)\right]-\alpha\right\}} \times \frac{0.61\lambda}{NA}, \tag{4.1}$$

where α is off-axis angle of the metalens. The resolution of the metalens-based spectrometer (2.9 nm) could be designed as a constant when shrinking the size of the device, which is essential for the compact integration. By employing the dispersion engineering, an aberration-corrected off-axis metalens-based spectrometer was also realized [201]. Metalens could also be designed as an independent camera by combining a CMOS detector [102]. As shown in Figure 7(a), the total size of the miniature optical camera is 1.6 mm × 1.6 mm × 1.7 mm, with a correcting metalens on the top to revise the monochromatic aberrations as introduced in Section 3. The modulation transfer function (MTF) that represents the relative contrast of the image and the spatial details shows that the cascaded doublet metalens could improve the diffraction limited performance. Such miniature camera design indicates the potential of portable metalens-based imaging devices. With an array of 60 × 60 small achromatic metalenses, a full-color light-field camera was also realized [202]. The building block of the metalens is gallium nitride unit element, which has been demonstrated capable of correcting the chromatic aberration in the visible [123]. Similar to the traditional light-field camera, the raw light-field image contains numerous sub-images due to the existence of the metalens array (Figure 7(b)). By rendering the images with different focusing depths, the three objects (the three letters A, B, and C) at different depths were reconstructed. Furthermore, the object in the scene could be reconstructed slice by slice with the corresponding rendered images. Taking advantages of the abilities of metasurface to manipulate polarizations of EMWs, researchers have realized a compact full-Stokes polarization camera [203]. As shown in Figure 7(c), a matrix metagrating was designed which could scatter different polarized copies of the transmitted images to four different quadrants. Thus, one could obtain four images of an object with different polarization information. By analyzing the raw images with different processes channels, such as S_0 (traditional intensity image), S_3 (the chiral Stokes component), the azimuth of the polarization ellipse, and the degree of polarization, the polarization information of the object could be visualized (Figure 7(c ii)). This method provides a promising approach for machine vision and materials detection such as the surface-stress-birefringence analysis. The researchers also achieved a portable prototype with adjustable focus of the full-Stokes polarization camera. There are some other good examples of the combination of metalenses and postprocessing algorithms. Recently, researchers developed a compact single-shot metalens depth sensor by mimicking the jumping spider [204]. As shown in Figure 7(d), the metalens simultaneously captures

two images with different defocus, and a postprocessing method was employed to obtain the depth map of the object with a single shot. The abovementioned metalens cameras are examples of current burgeoning developing photonic metalens-based techniques, and could potentially benefit future imaging and sensing areas.

5. Conclusions and outlook

In summary, with the innovation in fundamental design principles, the basic materials, and the manufacturing techniques, metalens has become a promising platform for future practical photonic devices. Herein, we have reviewed the design motivation, principles, and applications of diffractive metalens based on the wavefront manipulation of EMWs. We reviewed the diffractive performance of metalenses composed of different building blocks such as metallic, dielectric, 2D, and nonlinear materials. The phase in each unit cell is decided by the materials type, geometric design, and the symmetry of the nanostructures, leading to wavefront manipulations of EMWs pixel by pixel. We reviewed the basic metalens components such as monochromatic aberrations corrected metalens, achromatic metalens, subresolution metalens, nonlinear metalens, and AI-aided metalens. All of these metalens components are important in the understanding of metasurface designs and future applications. Currently, different kinds of high-performance metalenses have been developed step by step, and approach the practical applications day after day. We also reviewed several metalens systems such as the multifunctional metalens, tunable and reconfigurable metalens, and metalens cameras, which are challenging to realize with traditional optical designs. Recently, multi-level diffraction lens provides another way to realize ultrathin flat lens with high efficiency and shows inspiring potentials to correct the imaging aberrations [205–207]. The major difference between multi-level diffraction lens and metalens lies in local modes, considering both of the two types of lenses are based on diffractions in continuous media. Taking advantages of the abundant local resonance modes of sub-wavelength nanostructures, such as waveguide modes, Mie scattering modes and near-field modes, metalens provides the possibilities to manipulate the optical fields with high degree of freedom. On the other hand, as the development of fabrication techniques, many novel Quantum effects and modes such as Casimir effect and large nonlinearity are exploited [208,209]. We believe the rapid development of metalens will make a difference in future photonic and quantum techniques, at least partially replacing conventional optical devices.

There are some challenges to be overcome in the metalens design. For example, although the ultrahigh working NA metalens has been experimentally demonstrated, the aberration-free high NA metalens operating at large

field-of-view with high efficiency is still challenging. In this review, we also envision several directions in future metalens designs.

(1) *Sub-resolution metalens with improved efficiency, field-of-view, and minimized foci.*

Theoretically, the super-oscillatory sub-resolution focusing is a tradeoff among the focal size, working efficiency and the size of the field-of-view. As discussed in Section 3.3, a number of methods have been proposed to realize the label-free super-oscillatory metalens, which more or less suffered from some specific limitations. One of the possible solutions is by combining the multi-dimensional manipulation of the optical fields with judicious nanostructures design [31,210]. The figure of merit could also be improved by combining some postprocessing algorithms, instead of direct optimization of the multi-parameters in the metalens design, such as improving the field-of-view by multi-shots or composite combination of the sub-resolution images. Another promising method may be utilizing coherent or structured incident light [9,211]. Taking advantages of the versatile abilities of the metalens and its high design degree of freedom, metalens provides a promising platform for practical label-free sub-resolution imaging techniques.

(2) *AI-aided high-performance metalens.*

Compared with the bulky size of traditional optical devices and microscopy, metalens enables focusing and imaging on a compact size with multi-functions. Recently, the rapid development of functional metalens-based cameras provides potentials for integrated metalens systems, which combine numerous metalens components or functions all together. How to design and to optimize such metalens systems and how to postprocess the vast captured images remain questions. Recently, AI techniques have drawn much attention in both commercial and the scientific community [155,161,212–214], and may enable the realization of super-resolution imaging, photonic quantum computing, and a plenty of intriguing branches. AI techniques even provide possibilities for loop-locked design from materials choosing, geometric design, array arrangement, to fabrication processes, which may give birth to future high-performance metalenses and corresponding systems.

(3) *Reconfigurable full-control metalens with high response speed.*

Tunable and reconfigurable metasurfaces have been widely investigated in various wavebands based on electrical, magnetical, thermal, mechanical, chemical, optical and many other inducing methods. To date, it is still challenging to realize full dynamic control of the wavefront pixel by pixel in the metasurface platform, especially in the near infrared and in the visible region, since the scale of the dynamic tuning operation is limited in various ways. For example, for optical tuning methods the tuning areas are restricted by the diffraction limit, and for electrical tuning methods the tuning areas are limited by the size of the electrodes or switches. For

metalens, it is feasible to adjust the focal length through doublet method without tuning the phase in each unit cell [196], but the full dynamic control of the phase in each unit cell allows much more potential designs such as multifunctional and integrated reconfigurable metalens. On the other hand, how to increase the response speed of the reconfigurable metalens is also a key point in metalens-based scanning and imaging devices.

Disclosure Statement

No potential conflict of interest was reported by the authors.

Funding

This work was supported by the National Key Research and Development Program of China [Grant Nos. 2016YFA0301102 and 2017YFA0303800], the National Natural Science Fund for Distinguished Young Scholar [11925403], the National Natural Science Foundation of China [Grant Nos. 11974193, 11904181, 11904183, 91856101, and 11774186], the Natural Science Foundation of Tianjin for Distinguished Young Scientists [Grant No. 18JCJQJC45700], the National Postdoctoral Program for Innovative Talents [Grant No. BX20180148], the China Postdoctoral Science Foundation [Grant Nos. 2018M640229 and 2018M640224], and 111 Project [Grant No. B07013].

References

[1] Saleh BEA, Teich MC. Fundamental of photonics. New York: John Wiley & Sons; 1991.
[2] Monticone F, Alù A. Metamaterial, plasmonic and nanophotonic devices. Rep Prog Phys. 2017;80:036401.
[3] Chen H-T, Taylor AJ, Yu N. A review of metasurfaces: physics and applications. Rep Prog Phys. 2016;79:076401.
[4] Chen S, Li Z, Liu W, et al. From single-dimensional to multidimensional manipulation of optical waves with metasurfaces. Adv Mater. 2019;31:1802458.
[5] Liu S, Cui TJ. Concepts, working principles, and applications of coding and programmable metamaterials. Adv Opt Mater. 2017;5:1700624.
[6] Berry M, Zheludev N, Aharonov Y, et al. Roadmap on superoscillations. J Optics-Uk. 2019;21:053002.
[7] Bek A, Vogelgesang R, Kern K. Apertureless scanning near field optical microscope with sub-10nm resolution. Rev Sci Instrum. 2006;77:043703.
[8] Betzig E, Patterson GH, Sougrat R, et al. Imaging intracellular fluorescent proteins at nanometer resolution. Science. 2006;313:1642.
[9] Gustafsson MGL. Nonlinear structured-illumination microscopy: wide-field fluorescence imaging with theoretically unlimited resolution. Proc Natl Acad Sci. 2005;102:13081.
[10] Klar TA, Hell SW. Subdiffraction resolution in far-field fluorescence microscopy. Opt Lett. 1999;24:954–956.
[11] Rust MJ, Bates M, Zhuang X. Sub-diffraction-limit imaging by stochastic optical reconstruction microscopy (storm). Nat Methods. 2006;3:793–795.

[12] Szameit A, Shechtman Y, Osherovich E, et al. Sparsity-based single-shot subwavelength coherent diffractive imaging. Nat Mater. 2012;11:455–459.
[13] Sheppard CJR, Choudhury A. Annular pupils, radial polarization, and superresolution. Appl Optics. 2004;43:4322–4327.
[14] Roy T, Rogers ETF, Zheludev NI. Sub-wavelength focusing meta-lens. Opt Express. 2013;21:7577–7582.
[15] Yu N, Genevet P, Kats MA, et al. Light propagation with phase discontinuities: generalized laws of reflection and refraction. Science. 2011;334:333–337.
[16] Zhou H, Peng C, Yoon Y, et al. Observation of bulk Fermi arc and polarization half charge from paired exceptional points. Science. 2018;359:1009–1012.
[17] Srivastava YK, Manjappa M, Cong L, et al. A superconducting dual-channel photonic switch. Adv Mater. 2018;30:1801257.
[18] Miri MA, Alù A. Exceptional points in optics and photonics. Science. 2019;363: eaar7709.
[19] Huang L, Chen X, Mühlenbernd H, et al. Dispersionless phase discontinuities for controlling light propagation. Nano Lett. 2012;12:5750–5755.
[20] Mutlu M, Akosman AE, Serebryannikov AE, et al. Diodelike asymmetric transmission of linearly polarized waves using magnetoelectric coupling and electromagnetic wave tunneling. Phys Rev Lett. 2012;108:213905.
[21] Kaelberer T, Fedotov VA, Papasimakis N, et al. Toroidal dipolar response in a metamaterial. Science. 2010;330:1510–1512.
[22] Grinblat G, Li Y, Nielsen MP, et al. Efficient third harmonic generation and nonlinear subwavelength imaging at a higher-order anapole mode in a single germanium nanodisk. ACS Nano. 2017;11:953–960.
[23] Deng ZL, Deng J, Zhuang X, et al. Facile metagrating holograms with broadband and extreme angle tolerance. Light Sci Appl. 2018;7:78.
[24] Jang M, Horie Y, Shibukawa A, et al. Wavefront shaping with disorder-engineered metasurfaces. Nat Photon. 2018;12:84–90.
[25] Yang Y, Wang W, Moitra P, et al. Dielectric meta-reflectarray for broadband linear polarization conversion and optical vortex generation. Nano Lett. 2014;14:1394–1399.
[26] Liu WW, Chen SQ, Li ZC, et al. Realization of broadband cross-polarization conversion in transmission mode in the terahertz region using a single-layer metasurface. Opt Lett. 2015;40:3185–3188.
[27] Qian Q, Sun T, Yan Y, et al. Large-area wide-incident-angle metasurface perfect absorber in total visible band based on coupled Mie resonances. Adv Opt Mater. 2017;5:1700064.
[28] Liu N, Mesch M, Weiss T, et al. Infrared perfect absorber and its application as plasmonic sensor. Nano Lett. 2010;10:2342–2348.
[29] Chen SQ, Cheng H, Yang HF, et al. Polarization insensitive and omnidirectional broadband near perfect planar metamaterial absorber in the near infrared regime. Appl Phys Lett. 2011;99:253104.
[30] Cheng H, Chen SQ, Yu P, et al. Dynamically tunable plasmonically induced transparency in periodically patterned graphene nanostrips. Appl Phys Lett. 2013;103:203112.
[31] Xu H-X, Hu G, Han L, et al. Chirality-assisted high-efficiency metasurfaces with independent control of phase, amplitude, and polarization. Adv Opt Mater. 2018;6:1801479.
[32] Balthasar Mueller JP, Rubin NA, Devlin RC, et al. Metasurface polarization optics: independent phase control of arbitrary orthogonal states of polarization. Phys Rev Lett. 2017;118:113901.

[33] Devlin RC, Ambrosio A, Rubin NA, et al. Arbitrary spin-to-orbital angular momentum conversion of light. Science. 2017;358:896–901.
[34] Arbabi A, Horie Y, Bagheri M, et al. Dielectric metasurfaces for complete control of phase and polarization with subwavelength spatial resolution and high transmission. Nat Nanotechnol. 2015;10:937–943.
[35] Li JX, Chen SQ, Yang HF, et al. Simultaneous control of light polarization and phase distributions using plasmonic metasurfaces. Adv Funct Mater. 2015;25:704–710.
[36] Pfeiffer C, Emani NK, Shaltout AM, et al. Efficient light bending with isotropic metamaterial Huygens' surfaces. Nano Lett. 2014;14:2491–2497.
[37] Zhang X, Tian Z, Yue W, et al. Broadband terahertz wave deflection based on C-shape complex metamaterials with phase discontinuities. Adv Mater. 2013;25:4567–4572.
[38] Yin X, Ye Z, Rho J, et al. Photonic spin Hall effect at metasurfaces. Science. 2013;339:1405–1407.
[39] Genevet P, Wintz D, Ambrosio A, et al. Controlled steering of Cherenkov surface plasmon wakes with a one-dimensional metamaterial. Nat Nanotechnol. 2015;10:804–809.
[40] Pfeiffer C, Grbic A. Controlling vector Bessel beams with metasurfaces. Phys Rev Appl. 2014;2:044012.
[41] Li Z, Cheng H, Liu ZC, et al. Plasmonic Airy beam generation by both phase and amplitude modulation with metasurfaces. Adv Opt Mater. 2016;4:1230–1235.
[42] Yu N, Aieta F, Genevet P, et al. A broadband, background-free quarter-wave plate based on plasmonic metasurfaces. Nano Lett. 2012;12:6328–6333.
[43] Li Z, Kim MH, Wang C, et al. Controlling propagation and coupling of waveguide modes using phase-gradient metasurfaces. Nat Nanotechnol. 2017;12:675–683.
[44] Wu S, Zhang Z, Zhang Y, et al. Enhanced rotation of the polarization of a light beam transmitted through a silver film with an array of perforated S-shaped holes. Phys Rev Lett. 2013;110:207401.
[45] Pfeiffer C, Grbic A. Metamaterial Huygens' surfaces: tailoring wave fronts with reflectionless sheets. Phys Rev Lett. 2013;110:197401.
[46] Wang Y, Fang X, Kuang Z, et al. On-chip generation of broadband high-order Laguerre-Gaussian modes in a metasurface. Opt Lett. 2017;42:2463–2466.
[47] Wong AMH, Eleftheriades GV. Perfect anomalous reflection with a bipartite Huygens' metasurface. Phys Rev X. 2018;8:011036.
[48] Yu P, Li JX, Tang CC, et al. Controllable optical activity with non-chiral plasmonic metasurfaces. Light-Sci Appl. 2016;5:e16096.
[49] Liu ZC, Li ZC, Liu Z, et al. High-performance broadband circularly polarized beam deflector by mirror effect of multinanorod metasurfaces. Adv Funct Mater. 2015;25:5428–5434.
[50] Campione S, Basilio LI, Warne LK, et al. Tailoring dielectric resonator geometries for directional scattering and Huygens' metasurfaces. Opt Express. 2015;23:2293–2307.
[51] Zhan A, Gibson R, Whitehead J, et al. Controlling three-dimensional optical fields via inverse Mie scattering. Sci Adv. 2019;5:eaax4769.
[52] Liu S, Vaskin A, Campione S, et al. Huygens' metasurfaces enabled by magnetic dipole resonance tuning in split dielectric nanoresonators. Nano Lett. 2017;17:4297–4303.
[53] Yang B, Liu W, Li Z, et al. Ultrahighly saturated structural colors enhanced by multipolar-modulated metasurfaces. Nano Lett. 2019;19:4221–4228.
[54] Jahani S, Jacob Z. All-dielectric metamaterials. Nat Nanotechnol. 2016;11:23–36.
[55] Staude I, Schilling J. Metamaterial-inspired silicon nanophotonics. Nat Photon. 2017;11:274–284.

[56] Lin D, Fan P, Hasman E, et al. Dielectric gradient metasurface optical elements. Science. 2014;345:298–302.
[57] Khorasaninejad M, Crozier KB. Silicon nanofin grating as a miniature chirality-distinguishing beam-splitter. Nat Commun. 2014;5:5386.
[58] Li P, Dolado I, Alfaro-Mozaz FJ, et al. Infrared hyperbolic metasurface based on nanostructured Van der Waals materials. Science. 2018;359:892.
[59] Cheng H, Chen S, Yu P, et al. Dynamically tunable broadband infrared anomalous refraction based on graphene metasurfaces. Adv Opt Mater. 2015;3:1744–1749.
[60] Li ZC, Liu WW, Cheng H, et al. Tunable dual-band asymmetric transmission for circularly polarized waves with graphene planar chiral metasurfaces. Opt Lett. 2016;41:3142–3145.
[61] Pendry JB, Huidobro PA, Luo Y, et al. Compacted dimensions and singular plasmonic surfaces. Science. 2017;358:915–917.
[62] Zhang Y, Liu W, Li Z, et al. Ultrathin polarization-insensitive wide-angle broadband near-perfect absorber in the visible regime based on few-layer MoS_2 films. Appl Phys Lett. 2017;111:111109.
[63] Yoon G, Lee D, Nam KT, et al. "Crypto-display" in dual-mode metasurfaces by simultaneous control of phase and spectral responses. ACS Nano. 2018;12:6421–6428.
[64] Huang LL, Chen XZ, Bai BF, et al. Helicity dependent directional surface plasmon polariton excitation using a metasurface with interfacial phase discontinuity. Light Sci Appl. 2013;2:e70.
[65] Cong LQ, Srivastava YK, Zhang HF, et al. All-optical active THz metasurfaces for ultrafast polarization switching and dynamic beam splitting. Light Sci Appl. 2018;7:1–9.
[66] Ding X, Monticone F, Zhang K, et al. Ultrathin Pancharatnam-Berry metasurface with maximal cross-polarization efficiency. Adv Mater. 2015;27:1195–1200.
[67] Aieta F, Genevet P, Kats MA, et al. Aberration-free ultrathin flat lenses and axicons at telecom wavelengths based on plasmonic metasurfaces. Nano Lett. 2012;12:4932–4936.
[68] Grady NK, Heyes JE, Chowdhury DR, et al. Terahertz metamaterials for linear polarization conversion and anomalous refraction. Science. 2013;340:1304–1307.
[69] Huang YW, Chen WT, Wu PC, et al. Design of plasmonic toroidal metamaterials at optical frequencies. Opt Express. 2012;20:1760–1768.
[70] Liu M, Choi DY. Extreme Huygens' metasurfaces based on quasi-bound states in the continuum. Nano Lett. 2018;18:8062–8069.
[71] Huang K, Qin F, Liu H, et al. Planar diffractive lenses: fundamentals, functionalities, and applications. Adv Mater. 2018;30:e1704556.
[72] Khorasaninejad M, Zhu AY, Roques-Carmes C, et al. Polarization-insensitive metalenses at visible wavelengths. Nano Lett. 2016;16:7229–7234.
[73] Liu W, Li Z, Cheng H, et al. Momentum analysis for metasurfaces. Phys Rev Appl. 2017;8:014012.
[74] Bomzon Z, Kleiner V, Hasman E. Pancharatnam–Berry phase in space-variant polarization-state manipulations with subwavelength gratings. Opt Lett. 2001;26:1424–1426.
[75] Chen X, Huang L, Muhlenbernd H, et al. Dual-polarity plasmonic metalens for visible light. Nat Commun. 2012;3:1198.
[76] Ding F, ZX W, SL H, et al. Broadband high-efficiency half-wave plate: a supercell-based plasmonic metasurface approach. ACS Nano. 2015;9:4111–4119.
[77] Li ZC, Liu WW, Cheng H, et al. Manipulation of the photonic spin Hall effect with high efficiency in gold-nanorod-based metasurfaces. Adv Opt Mater. 2017;5:1700413.

[78] Liu W, Li Z, Li Z, et al. Energy-tailorable spin-selective multifunctional metasurfaces with full Fourier components. Adv Mater. 2019;31:1901729.
[79] Kruk S, Hopkins B, Kravchenko II, et al. Invited article: broadband highly efficient dielectric metadevices for polarization control. APL Photonics. 2016;1:030801.
[80] Chen S, Li Z, Zhang Y, et al. Phase manipulation of electromagnetic waves with metasurfaces and its applications in nanophotonics. Adv Opt Mater. 2018;6:1800104.
[81] Khorasaninejad M, Chen WT, Devlin RC, et al. Metalenses at visible wavelengths: diffraction-limited focusing and subwavelength resolution imaging. Science. 2016;352:1190–1194.
[82] Fan Z-B, Shao Z-K, Xie M-Y, et al. Silicon nitride metalenses for close-to-one numerical aperture and wide-angle visible imaging. Phys Rev Appl. 2018;10:014005.
[83] Devlin RC, Khorasaninejad M, Chen WT, et al. Broadband high-efficiency dielectric metasurfaces for the visible spectrum. Proc Natl Acad Sci. 2016;113:10473–10478.
[84] Khorasaninejad M, Ambrosio A, Kanhaiya P, et al. Broadband and chiral binary dielectric meta-holograms. Sci Adv. 2016;2:e1501258.
[85] Cheng JR, Jafar-Zanjani S, Mosallaei H. All-dielectric ultrathin conformal metasurfaces: lensing and cloaking applications at 532 nm wavelength. Sci Rep. 2016;6:38440.
[86] Genevet P, Capasso F, Aieta F, et al. Recent advances in planar optics: from plasmonic to dielectric metasurfaces. Optica. 2017;4:139.
[87] Kuznetsov AI, Miroshnichenko AE, Brongersma ML, et al. Optically resonant dielectric nanostructures. Science. 2016;354:aag2472.
[88] Khorasaninejad M, Chen WT, Zhu AY, et al. Multispectral chiral imaging with a metalens. Nano Lett. 2016;16:4595–4600.
[89] Zhu AY, Chen WT, Zaidi A, et al. Giant intrinsic chiro-optical activity in planar dielectric nanostructures. Light Sci Appl. 2018;7:17158.
[90] Zhang F, Pu M, Li X, et al. All-dielectric metasurfaces for simultaneous giant circular asymmetric transmission and wavefront shaping based on asymmetric photonic spin-orbit interactions. Adv Funct Mater. 2017;27:1704295.
[91] Wang B, Dong F, Yang D, et al. Polarization-controlled color-tunable holograms with dielectric metasurfaces. Optica. 2017;4:1368.
[92] Khorasaninejad M, Capasso F. Metalenses: versatile multifunctional photonic components. Science. 2017;358:eaam8100.
[93] Zhang Y, Liu W, Li Z, et al. High-quality-factor multiple fano resonances for refractive index sensing. Opt Lett. 2018;43:1842–1845.
[94] Liang H, Lin Q, Xie X, et al. Ultrahigh numerical aperture metalens at visible wavelengths. Nano Lett. 2018;18:4460–4466.
[95] Liu W, Li Z, Cheng H, et al. Metasurface enabled wide-angle Fourier lens. Adv Mater. 2018;30:1706368.
[96] Qiu M, Jia M, Ma S, et al. Angular dispersions in terahertz metasurfaces: physics and applications. Phys Rev Appl. 2018;9:054050.
[97] Kamali SM, Arbabi E, Arbabi A, et al. Angle-multiplexed metasurfaces: encoding independent wavefronts in a single metasurface under different illumination angles. Phys Rev X. 2017;7:041056.
[98] Estakhri NM, Neder V, Knight MW, et al. Visible light, wide-angle graded metasurface for back reflection. ACS Photonics. 2017;4:228–235.
[99] Guo YH, Ma XL, Pu MB, et al. High-efficiency and wide-angle beam steering based on catenary optical fields in ultrathin metalens. Adv Opt Mater. 2018;6:1800592.
[100] Pu M, Li X, Guo Y, et al. Nanoapertures with ordered rotations: symmetry transformation and wide-angle flat lensing. Opt Express. 2017;25:31471.

[101] Wen D, Yue F, Ardron M, et al. Multifunctional metasurface lens for imaging and Fourier transform. Sci Rep. 2016;6:27628.
[102] Arbabi A, Arbabi E, Kamali SM, et al. Miniature optical planar camera based on a wide-angle metasurface doublet corrected for monochromatic aberrations. Nat Commun. 2016;7:13682.
[103] Groever B, Chen WT, Capasso F. Metalens doublet in the visible region. Nano Lett. 2017;17:4902–4907.
[104] Pendry JB. Negative refraction makes a perfect lens. Phys Rev Lett. 2000;85:3966–3969.
[105] Xu T, Agrawal A, Abashin M, et al. All-angle negative refraction and active flat lensing of ultraviolet light. Nature. 2013;497:470–474.
[106] Kaina N, Lemoult F, Fink M, et al. Negative refractive index and acoustic superlens from multiple scattering in single negative metamaterials. Nature. 2015;525:77–81.
[107] Monticone F, Valagiannopoulos CA, Alù A. Parity-time symmetric nonlocal metasurfaces: all-angle negative refraction and volumetric imaging. Phys Rev X. 2016;6:041018.
[108] Aieta F, Kats MA, Genevet P, et al. Multiwavelength achromatic metasurfaces by dispersive phase compensation. Science. 2015;347:1342–1345.
[109] Avayu O, Almeida E, Prior Y, et al. Composite functional metasurfaces for multispectral achromatic optics. Nat Commun. 2017;8:14992.
[110] Cheng H, Liu ZC, Chen SQ, et al. Emergent functionality and controllability in few-layer metasurfaces. Adv Mater. 2015;27:5410–5421.
[111] Zhang J, ElKabbash M, Wei R, et al. Plasmonic metasurfaces with 42.3% transmission efficiency in the visible. Light Sci Appl. 2019;8:53.
[112] Frese D, Wei Q, Wang Y, et al. Nonreciprocal asymmetric polarization encryption by layered plasmonic metasurfaces. Nano Lett. 2019;19:3976–3980.
[113] Luo X. Subwavelength optical engineering with metasurface waves. Adv Opt Mater. 2018;6:1701201.
[114] Arbabi A, Arbabi E, Horie Y, et al. Planar metasurface retroreflector. Nat Photon. 2017;11:415.
[115] Chen S, Zhang Y, Li Z, et al. Empowered layer effects and prominent properties in few-layer metasurfaces. Adv Opt Mater. 2019;7:1801477.
[116] Khorasaninejad M, Shi Z, Zhu AY, et al. Achromatic metalens over 60 nm bandwidth in the visible and metalens with reverse chromatic dispersion. Nano Lett. 2017;17:1819–1824.
[117] Chen BH, Wu PC, Su VC, et al. GaN metalens for pixel-level full-color routing at visible light. Nano Lett. 2017;17:6345–6352.
[118] Khorasaninejad M, Aieta F, Kanhaiya P, et al. Achromatic metasurface lens at telecommunication wavelengths. Nano Lett. 2015;15:5358–5362.
[119] Arbabi E, Arbabi A, Kamali SM, et al. Multiwavelength polarization-insensitive lenses based on dielectric metasurfaces with meta-molecules. Optica. 2016;3:628.
[120] Wang S, Wu PC, Su VC, et al. Broadband achromatic optical metasurface devices. Nat Commun. 2017;8:187.
[121] Chen WT, Zhu AY, Sisler J, et al. Broadband achromatic metasurface-refractive optics. Nano Lett. 2018;18:7801–7808.
[122] Chen WT, Zhu AY, Sanjeev V, et al. A broadband achromatic metalens for focusing and imaging in the visible. Nat Nanotechnol. 2018;13:220–226.
[123] Wang S, Wu PC, Su VC, et al. A broadband achromatic metalens in the visible. Nat Nanotechnol. 2018;13:227–232.
[124] Chen G, Wen ZQ, Qiu CW. Superoscillation: from physics to optical applications. Light Sci Appl. 2019;8:56.

[125] Berry MV, Popescu S. Evolution of quantum superoscillations and optical super-resolution without evanescent waves. J Phys A. 2006;39:6965–6977.
[126] Dorn R, Quabis S, Leuchs G. Sharper focus for a radially polarized light beam. Phys Rev Lett. 2003;91:233901.
[127] Wang H, Shi L, Lukyanchuk B, et al. Creation of a needle of longitudinally polarized light in vacuum using binary optics. Nat Photon. 2008;2:501–505.
[128] Liu T, Tan J, Liu J, et al. Vectorial design of super-oscillatory lens. Opt Express. 2013;21:15090–15101.
[129] Maucher F, Skupin S, Gardiner SA, et al. Creating complex optical longitudinal polarization structures. Phys Rev Lett. 2018;120:163903.
[130] Huang K, Ye H, Teng J, et al. Optimization-free superoscillatory lens using phase and amplitude masks. Laser Photonics Rev. 2014;8:152–157.
[131] Qin F, Huang K, Wu J, et al. Shaping a subwavelength needle with ultra-long focal length by focusing azimuthally polarized light. Sci Rep. 2015;5:9977.
[132] Diao J, Yuan W, Yu Y, et al. Controllable design of super-oscillatory planar lenses for sub-diffraction-limit optical needles. Opt Express. 2016;24:1924–1933.
[133] Huang FM, Zheludev NI. Super-resolution without evanescent waves. Nano Lett. 2009;9:1249–1254.
[134] Li Z, Zhang T, Wang YQ, et al. Achromatic broadband super-resolution imaging by super-oscillatory metasurface. Laser Photonics Rev. 2018;12:1800064.
[135] Yuan GH, Rogers KS, Rogers ETF, et al. Far-field superoscillatory metamaterial superlens. Phys Rev Appl. 2019;11:064016.
[136] Lawrence M, Barton DR 3rd, Dionne JA. Nonreciprocal flat optics with silicon metasurfaces. Nano Lett. 2018;18:1104–1109.
[137] Zuo R, Liu W, Cheng H, et al. Breaking the diffraction limit with radially polarized light based on dielectric metalenses. Adv Opt Mater. 2018;6:1800795.
[138] Li Y, Cao L, Wen Z, et al. Broadband quarter-wave birefringent meta-mirrors for generating sub-diffraction vector fields. Opt Lett. 2019;44:110–113.
[139] Chen S, Li G, Zeuner F, et al. Symmetry-selective third-harmonic generation from plasmonic metacrystals. Phys Rev Lett. 2014;113:033901.
[140] Lepetit T, Kanté B. Nonlinear optics: metamaterial quasi-phase matching. Nat Photon. 2015;9:148–150.
[141] Li G, Chen S, Pholchai N, et al. Continuous control of the nonlinearity phase for harmonic generations. Nat Mater. 2015;14:607–612.
[142] Segal N, Keren-Zur S, Hendler N, et al. Controlling light with metamaterial-based nonlinear photonic crystals. Nat Photon. 2015;9:180–184.
[143] Tymchenko M, Gomez-Diaz JS, Lee J, et al. Gradient nonlinear Pancharatnam-Berry metasurfaces. Phys Rev Lett. 2015;115:207403.
[144] Chen S, Zeuner F, Weismann M, et al. Giant nonlinear optical activity of achiral origin in planar metasurfaces with quadratic and cubic nonlinearities. Adv Mater. 2016;28:2992–2999.
[145] Ye W, Zeuner F, Li X, et al. Spin and wavelength multiplexed nonlinear metasurface holography. Nat Commun. 2016;7:11930.
[146] Li G, Zhang S, Zentgraf T. Nonlinear photonic metasurfaces. Nat Rev Mater. 2017;2:17010.
[147] Rahimi E, Gordon R. Nonlinear plasmonic metasurfaces. Adv Opt Mater. 2018;6:1800274.
[148] Schlickriede C, Waterman N, Reineke B, et al. Imaging through nonlinear metalens using second harmonic generation. Adv Mater. 2018;30:1703843.

[149] Li G, Zentgraf T, Zhang S. Rotational Doppler effect in nonlinear optics. Nat Phys. 2016;12:736–740.
[150] Li G, Wu L, Li KF, et al. Nonlinear metasurface for simultaneous control of spin and orbital angular momentum in second harmonic generation. Nano Lett. 2017;17:7974–7979.
[151] Hafez HA, Kovalev S, Deinert JC, et al. Extremely efficient terahertz high-harmonic generation in graphene by hot Dirac fermions. Nature. 2018;561:507–511.
[152] Liu S, Vabishchevich PP, Vaskin A, et al. An all-dielectric metasurface as a broadband optical frequency mixer. Nat Commun. 2018;9:2507.
[153] Chen J, Wang K, Long H, et al. Tungsten disulfide-gold nanohole hybrid metasurfaces for nonlinear metalenses in the visible region. Nano Lett. 2018;18:1344–1350.
[154] Hu GW, Hong XM, Wang K, et al. Coherent steering of nonlinear chiral valley photons with a synthetic Au-WS_2 metasurface. Nat Photon. 2019;13:467–472.
[155] Ma W, Cheng F, Liu YM. Deep-learning-enabled on-demand design of chiral metamaterials. ACS Nano. 2018;12:6326–6334.
[156] Won R. Intelligent learning with light. Nat Photon. 2018;12:570–571.
[157] Bonod N, Bidault S, Burr GW, et al. Evolutionary optimization of all-dielectric magnetic nanoantennas. Adv Opt Mater. 2019;7:1900121.
[158] Pinkard H, Phillips Z, Babakhani A, et al. Deep learning for single-shot autofocus microscopy. Optica. 2019;6:794–797.
[159] Qiu T, Shi X, Wang J, et al. Deep learning: A rapid and efficient route to automatic metasurface design. Adv Sci (Weinh). 2019;6:1900128.
[160] Yao K, Unni R, Zheng YB. Intelligent nanophotonics: merging photonics and artificial intelligence at the nanoscale. Nanophotonics-Berlin. 2019;8:339–366.
[161] Li L, Ruan H, Liu C, et al. Machine-learning reprogrammable metasurface imager. Nat Commun. 2019;10:1082.
[162] Liu Z, Zhu D, Rodrigues SP, et al. Generative model for the inverse design of metasurfaces. Nano Lett. 2018;18:6570–6576.
[163] Wiecha PR, Arbouet A, Girard C, et al. Evolutionary multi-objective optimization of colour pixels based on dielectric nanoantennas. Nat Nanotechnol. 2017;12:163–169.
[164] Phan T, Sell D, Wang EW, et al. High-efficiency, large-area, topology-optimized metasurfaces. Light Sci Appl. 2019;8:48.
[165] Chung H, Miller OD. High-NA achromatic metalenses by inverse design. Opt Express. 2020;28:6945–6965.
[166] Maguid E, Yulevich I, Veksler D, et al. Photonic spin-controlled multifunctional shared-aperture antenna array. Science. 2016;352:1202–1206.
[167] Jin J, Pu M, Wang Y, et al. Multi-channel vortex beam generation by simultaneous amplitude and phase modulation with two-dimensional metamaterial. Adv Mater Technol. 2017;2:1600201.
[168] Li Y, Li X, Chen L, et al. Orbital angular momentum multiplexing and demultiplexing by a single metasurface. Adv Opt Mater. 2017;5:1600502.
[169] Maguid E, Yulevich I, Yannai M, et al. Multifunctional interleaved geometric phase dielectric metasurfaces. Light Sci Appl. 2017;6:e17027.
[170] Yue F, Wen D, Zhang C, et al. Multichannel polarization-controllable superpositions of orbital angular momentum states. Adv Mater. 2017;29:1603838.
[171] Malek SC, Ee HS, Agarwal R. Strain multiplexed metasurface holograms on a stretchable substrate. Nano Lett. 2017;17:3641–3645.
[172] Wang Q, Zhang X, Plum E, et al. Polarization and frequency multiplexed terahertz meta-holography. Adv Opt Mater. 2017;5:1700277.

[173] Wei Q, Huang L, Li X, et al. Broadband multiplane holography based on plasmonic metasurface. Adv Opt Mater. 2017;5:1700434.
[174] Cheng H, Wei X, Yu P, et al. Integrating polarization conversion and nearly perfect absorption with multifunctional metasurfaces. Appl Phys Lett. 2017;110:171903.
[175] Neshev D, Aharonovich I. Optical metasurfaces: new generation building blocks for multi-functional optics. Light Sci Appl. 2018;7:58.
[176] Li Z, Liu W, Li Z, et al. Nonlinear metasurfaces: tripling the capacity of optical vortices by nonlinear metasurface. Laser Photonics Rev. 2018;12:1870049.
[177] Chen X, Chen M, Mehmood Muhammad Q, et al. Longitudinal multifoci metalens for circularly polarized light. Adv Opt Mater. 2015;3:1201–1206.
[178] Gao S, Park CS, Zhou C, et al. Twofold polarization-selective all-dielectric trifoci metalens for linearly polarized visible light. Adv Opt Mater. 2019;7:1900883.
[179] Williams C, Montelongo Y, Wilkinson TD. Plasmonic metalens for narrowband dual-focus imaging. Adv Opt Mater. 2017;5:1700811.
[180] Gholipour B, Zhang J, MacDonald KF, et al. An all-optical, non-volatile, bidirectional, phase-change meta-switch. Adv Mater. 2013;25:3050–3054.
[181] Michel A-KU, Chigrin DN, TWW M, et al. Using low-loss phase-change materials for mid-infrared antenna resonance tuning. Nano Lett. 2013;13:3470–3475.
[182] Du KK, Li Q, Lyu YB, et al. Control over emissivity of zero-static-power thermal emitters based on phase-changing material GST. Light Sci Appl. 2017;6:e16194.
[183] Li T, Huang L, Liu J, et al. Tunable wave plate based on active plasmonic metasurfaces. Opt Express. 2017;25:4216–4226.
[184] Qu Y, Li Q, Du K, et al. Dynamic thermal emission control based on ultrathin plasmonic metamaterials including phase-changing material GST. Laser Photonics Rev. 2017;11:1700091.
[185] Qu Y, Li Q, Cai L, et al. Thermal camouflage based on the phase-changing material GST. Light Sci Appl. 2018;7:26.
[186] Bai W, Yang P, Huang J, et al. Near-infrared tunable metalens based on phase change material $Ge_2Se_2Te_5$. Sci Rep. 2019;9:5368.
[187] Chu CH, Tseng ML, Chen J, et al. Active dielectric metasurface based on phase-change medium. Laser Photonics Rev. 2016;10:986–994.
[188] Yin X, Steinle T, Huang L, et al. Beam switching and bifocal zoom lensing using active plasmonic metasurfaces. Light Sci Appl. 2017;6:e17016.
[189] Liu MK, Hwang HY, Tao H, et al. Terahertz-field-induced insulator-to-metal transition in vanadium dioxide metamaterial. Nature. 2012;487:345–348.
[190] Kim Y, Wu PC, Sokhoyan R, et al. Phase modulation with electrically tunable vanadium dioxide phase-change metasurfaces. Nano Lett. 2019;19:3961–3968.
[191] Yu P, Li J, Zhang S, et al. Dynamic Janus metasurfaces in the visible spectral region. Nano Lett. 2018;18:4584–4589.
[192] Thareja V, Kang JH, Yuan H, et al. Electrically tunable coherent optical absorption in graphene with ion gel. Nano Lett. 2015;15:1570–1576.
[193] Kim -T-T, Kim H, Kenney M, et al. Amplitude modulation of anomalously refracted terahertz waves with gated-graphene metasurfaces. Adv Opt Mater. 2018;6:1700507.
[194] She A, Zhang S, Shian S, et al. Adaptive metalenses with simultaneous electrical control of focal length, astigmatism, and shift. Sci Adv. 2018;4:eaap9957.
[195] H-S E, Agarwal R. Tunable metasurface and flat optical zoom lens on a stretchable substrate. Nano Lett. 2016;16:2818–2823.
[196] Arbabi E, Arbabi A, Kamali SM, et al. MEMS-tunable dielectric metasurface lens. Nat Commun. 2018;9:812.

[197] Papaioannou M, Plum E, Rogers ET, et al. All-optical dynamic focusing of light via coherent absorption in a plasmonic metasurface. Light Sci Appl. 2018;7:17157.
[198] Li L, Jun Cui T, Ji W, et al. Electromagnetic reprogrammable coding-metasurface holograms. Nat Commun. 2017;8:197.
[199] Sherrott MC, Hon PWC, Fountaine KT, et al. Experimental demonstration of >230 degrees phase modulation in gate-tunable graphene-gold reconfigurable mid-infrared metasurfaces. Nano Lett. 2017;17:3027–3034.
[200] Khorasaninejad M, Chen WT, Oh J, et al. Super-dispersive off-axis meta-lenses for compact high resolution spectroscopy. Nano Lett. 2016;16:3732–3737.
[201] Zhu AY, Chen WT, Sisler J, et al. Compact aberration-corrected spectrometers in the visible using dispersion-tailored metasurfaces. Adv Opt Mater. 2018;7:1801144.
[202] Lin RJ, Su VC, Wang S, et al. Achromatic metalens array for full-colour light-field imaging. Nat Nanotechnol. 2019;14:227–231.
[203] Rubin NA, D'Aversa G, Chevalier P, et al. Matrix fourier optics enables a compact full-Stokes polarization camera. Science. 2019;365:eaax1839.
[204] Guo Q, Shi Z, Huang Y-W, et al. Compact single-shot metalens depth sensors inspired by eyes of jumping spiders. Proc Nat Acad Sci. 2019;116:22959–22965.
[205] Banerji S, Meem M, Majumder A, et al. Single flat lens enabling imaging in the short-wave infra-red (SWIR) band. OSA Contin. 2019;2:2968–2974.
[206] Banerji S, Meem M, Majumder A, et al. Imaging with flat optics: metalenses or diffractive lenses? Optica. 2019;6:805–810.
[207] Banerji S, Meem M, Majumder A, et al. Imaging over an unlimited bandwidth with a single diffractive surface. Arxiv. 2019;1907:06251.
[208] Zhao RK, Li L, Yang S, et al. Stable Casimir equilibria and quantum trapping. Science. 2019;364:984–987.
[209] Qian HL, Li SL, Chen CF, et al. Large optical nonlinearity enabled by coupled metallic quantum wells. Light Sci Appl. 2019;8:13.
[210] Li Z, Liu W, Cheng H, et al. Arbitrary manipulation of light intensity by bilayer aluminum metasurfaces. Adv Opt Mater. 2019;7:1900260.
[211] Mandula O, Kielhorn M, Wicker K, et al. Line scan-structured illumination microscopy super-resolution imaging in thick fluorescent samples. Opt Express. 2012;20:24167–24174.
[212] Nichols JA, Herbert Chan HW, Baker MAB. Machine learning: applications of artificial intelligence to imaging and diagnosis. Biophys Rev. 2019;11:111–118.
[213] Liu Z, Yan S, Liu H, et al. Superhigh-resolution recognition of optical vortex modes assisted by a deep-learning method. Phys Rev Lett. 2019;123:183902.
[214] Hail CU, Michel AKU, Poulikakos D, et al. Optical metasurfaces: evolving from passive to adaptive. Adv Opt Mater. 2019;7:1801786.